Chalcophile-siderophile element systematics of hydrothermal pyrite from martian regolith breccia NWA 7533

Jean-Pierre Lorand, R.H. Hewins, M. Humayun, L. Remusat, B. Zanda, Carole La, S. Pont

Chalcophile-siderophile element systematics of hydrothermal pyrite from martian regolith breccia NWA 7533

Jean-Pierre Lorand[1], Hewins R.H.[2,3], Humayun M.[4], Remusat L.[2], Zanda B.[2], La C.[1], Pont S.[2]

1 Laboratoire de Planétologie et Géodynamique à Nantes, CNRS UMR 6112, Université de Nantes, 2 Rue de la Houssinère, BP 92208, 44322 Nantes Cédex 3, France.

2 Institut de Minéralogie, de Physique des Matériaux, et de Cosmochimie (IMPMC) - Sorbonne Université- Muséum National d'Histoire Naturelle, UPMC Université Paris 06, UMR CNRS 7590, IRD UMR 206, 61 rue Buffon, 75005 Paris, France.

3 Department of Earth & Planetary Sciences, Rutgers University, Piscataway, NJ 08854, USA.

4 Department of Earth, Ocean & Atmospheric Science and National High Magnetic Field Laboratory, Florida State University, Tallahassee, FL 32310, USA.

Corresponding author Jean-Pierre Lorand *Email address:* jean-pierre.lorand@univ-nantes.fr. *Phone number 33 2 51 12 54 63 ; Fax number: 33 2 51 12 52 68.*

Abstract: Unlike other martian meteorites studied so far, Martian regolith breccia NWA 7533 and paired meteorites that have sampled 4.4 Ga-old impact lithologies show only sulfides of hydrothermal origin (mostly pyrite (<1 vol.%) and scarce pyrrhotite). NWA 7533 pyrite has been analyzed for 25 chalcophile-siderophile trace elements with laser ablation-inductively coupled plasma mass spectrometer (LA-ICPMS). Micronuggets of highly siderophile elements-HSE (Os, Ir, Pt, Ru, Rh) along with occasional detection of Mo and Re were observed in half of the 52 analyzed crystals as random concentration spikes in time-resolved LA-ICPMS data. These nuggets are interpreted as variably altered remnants from repeated meteorite bombardment of the early martian crust, as are chondritic Ni/Co ratios of pyrite (10-20). Pyrite displays superchondritic S/Se (54,000 to 3,300) and Te/Se (0.3 - >1). The reasonably good positive correlation (R^2=0.72) between Se and Ni reflects a temperature control on the solubility of both elements. Apart from the chalcogens S, Se and Te, pyrite appears to be a minor contributor (<20%) to the whole-rock budget for both HSE (including Ni and Co) and chalcophile metals Ag, As, Au, Cu, Hg, Pb, Sb, Tl and Zn. This deficit can result from i) high (>400°C) temperature crystallization for NWA 7533 pyrite, as deduced from its Se and Ni contents, ii) magmatic sulfide-depletion of brecciated early martian crust, iii) precipitation from near neutral H_2S-HS-H_2O-rich hydrothermal fluids that did not provide halogen ligands for extensive transport of chalcophile-siderophile metals. It is suggested that the 1.4 Ga lithification event that precipitated hydrothermal pyrite left the chalcophile-siderophile element budget of the early martian crust nearly unmodified, except for S, Se and Te.

1. INTRODUCTION

Chalcophile and siderophile metals comprise nearly 30 different elements that in theory prefer sulfide or iron metal structures, respectively. Most elements that are siderophile are usually also somewhat chalcophile and vice versa so that they are conveniently grouped as chalcophile-siderophile elements. (e.g. Arculus and Delano, 1981). Because they are concentrated in metallic and sulfide minerals that are highly sensitive to differentiation processes, these elements provide insight into a wide range of planetary-scale properties such as composition of planetary building blocks, the physical conditions of core-mantle segregation, (Day et al., 2016, and references therein), impactor signatures in impact craters (e.g. Dressler and Reimold, 2001; Koeberl et al., 2012, and references therein) as well as exogenous components in brecciated meteorites (e.g. Goderis et al., 2012). However, primordial patterns can be modified by secondary processes (e.g., hydrothermal alteration, metamorphic overprint) because chalcophile-siderophile elements show highly variable mobility in hydrothermal fluids (Barnes, 1979, 2015 and references therein; Kaassalainen et al., 2015).

Siderophile element contents (Ir, Ni) were used to identify Martian regolith breccia NWA 7533 and paired samples (e.g. NWA 7034; NWA 7475) as impact breccia rather than volcanic breccia (Humayun et al., 2013). Their siderophile element contents require the equivalent of 3 wt% of CI chondrite impactors admixed into Pre-Noachian lithologies (4.4 Ga) (Wittmann et al., 2015; Goderis et al., 2016). Subsequently near-neutral, H_2S-HS-rich fluids precipitated accessory pyrite (<1 vol.%) and scarce pyrrhotite at minimum log fO_2 > FMQ (fayalite-magnetite-quartz) + 2 log units and maximum T of 500°C (Lorand et al., 2015). Hence, these meteorites provide an opportunity for examining how the chalcophile-siderophile element budget of the early martian crust was processed by hydrothermal fluids.

Pyrite is by far the most abundant hydrothermal sulfide now reported from the three most studied stones of the martian impact breccia (NWA 7034, Muttik et al., 2014; NWA 7475, Wittmann et al., 2015; and NWA 7533, Lorand et al., 2015). Any inference on impactor debris and compositional features of the hydrothermal fluids must be constrained at first by estimating the part played by pyrite in the bulk-rock chalcophile-siderophile element budget. A scanning electron microscope (SEM) study of several hundreds of NWA 7533 pyrite crystals identified two micronuggets of highly siderophile elements (HSE, Os-Ir) that could be impactor debris (Lorand et al., 2015). About one-third of the 350 EDX (energy dispersive X-ray emission) and electron microprobe analyses (EMPA) analyses performed on pyrite detected Ni (up to 4.5 wt.%) and some Co (up to 1800 ppm) with a few analyses displaying a loosely constant Ni/Co around 10, reminiscent of meteoritic metal compositions (Lorand et al., 2015). Copper, Zn and As were found by these authors to occur at concentration levels below detection limits of trace element analyses by EMPA (<77, <91 ppm and <117 ppm, respectively) and Se (>64 ppm) was detected only in the most Ni-rich grains in the same study.

The present paper reports a more comprehensive data set for 25 chalcophile-siderophile trace elements analyzed with LA-ICPMS in NWA 7533 pyrite. LA-ICPMS analyses provide much better reproducibility for trace elements (Cu, Zn, As, Se) and sensitivity compared to EMPA. To date, LA-ICPMS analyses of martian sulfides were reported only for magmatic sulfides from young (< 1 Ga) basaltic rocks (shergottites) by Baumgartner et al (2017). Our results for NWA 7533 pyrite is therefore the only trace element concentration data that are available for martian sulfides of indisputable hydrothermal origin. Although pyrite is not uncommon in some martian meteorites (Lorand et al., 2018 and references therein), it was always reported as grains occurring as complex intergrowth with pyrrhotite too small-sized to be suitable for LA-ICPMS analyses.

2. MAIN PETROGRAPHIC FEATURES OF NWA 7533

2.1. Lithology

The NWA 7533 regolith breccia has been studied in detail by Hewins et al (2013, 2014a), Humayun et al., (2013, 2016), Nemchin et al (2014), Beck et al (2015), Belluci et al (2015) and Leroux et al (2016); a comprehensive review was given by Hewins et al. (2017). This meteorite consists of a fine-grained inter-clast matrix (acronym ICM) containing lithic clasts of microbasalt, norite, monzonite and single minerals derived from these rocks and probably orthopyroxenite, as well as clast-laden impact melt rocks (CLIMR) and impact melt spherules.

Noritic clasts consist of ferroan pyroxene ($En_{<72}$), orthopyroxene or inverted pigeonite, plagioclase (An_{50-30}) and Cr-rich magnetite. Monzonitic clasts show alkali feldspar, often perthitic, associated with plagioclase (An<30), ferroan pyroxene, chlorapatite and magnetite+ilmenite+ accessory rutile. Zircon and baddeleyite are found in these highly fractionated rock clasts, and also as individual mineral clasts. Zircon in monzonitic clasts gave a Pre-Noachian, U-Pb crystallization age of 4,423±26 Myr (1 sigma level; Humayun et al., 2013). Crystal clasts are fragments of disaggregated lithic clasts. The most magnesian orthopyroxene (En_{80-73}) is never attached to plagioclase, though associated with chrome spinel and rarely augite. It most probably derives from orthopyroxenites, perhaps pristine crustal rocks of the early Martian crust as suggested by its very low (<50 ppm) Ni concentrations (Hewins et al., 2014a). By contrast, noritic and monzonitic clasts contain high levels of siderophile elements (up to 1,000 ppm Ni, 1 <Ir <10 ppb) that indicate impactor-derived contamination (Humayun et al., 2013). The pervasive siderophile enrichment even in the melt rocks suggests a thick sequence of impact-generated rocks including mature regolith. Pyroxenes are either deep-seated clasts containing exsolution, or zoned pyroxenes of near surface origin.

Clast-laden melt rocks (CLMR) are dominated by plagioclase laths and subophitic pyroxene. Fine-grained basalt clasts (Hewins et al., 2013) with subophitic to granoblastic textures, grain size ~20-100 μm, are composed of orthopyroxene (En_{73-63}) or pigeonite (En_{63-49}) augite (En_{46-29}), plagioclase (An_{66-30}) and Fe-rich spinel. Their bulk compositions are close to those of the clast-laden ~~impact~~ melt rocks, including even higher contents of Ir (up to 100 ppb) (Humayun et al., 2013). They are interpreted as impact melt that crystallized less rapidly than CLMR, which were quenched more rapidly due to incorporation of abundant clasts. Regarding lithophile trace element geochemistry, the spherules, the groundmass of the melt rock and the microbasalts resemble melted wind blown dust and regolith debris (Humayun et al., 2013). The chemical composition of the fine-grained material in both the clasts and in the interclast matrix is very similar and was modeled as derived from crystallization products from a low-degree partial melt (<5%) of a chondritic garnet peridotite source (Humayun et al., 2013). The dense nanocrystalline matrix looks like annealed wind-blown dust with a granoblastic texture (Hewins et al., 2013; Muttik et al., 2014; Leroux et al., 2016). It consists of anhedral micrometer-sized plagioclase with sub-micrometer sized pyroxene

surrounding and embedded in it, plus fine-grained Fe-(Ti) oxides - magnetite, often symplectitic or lacy, and maghemite. The annealing and lithification process is related to a probable major reheating at 1.35–1.4 Ga which was recorded by several isotopic systems (see more details in McCubbin et al. (2016) and Hewins et al., 2017; Cassata et al., 2018). Some zircon grains show discordant ages corresponding to annealing at ~1.7–1.4 Ga (Humayun et al. 2013). The alkali-feldspars in leucocratic clasts record a very short-lived resetting event or mixing between feldspars and the whole rock at 1.4 Ga, and Pb-Pb age resetting at 1.36-1.45 Ga was documented in phosphates from all matrix domains of NWA 7034 and NWA 7533 (Bellucci et al., 2015). Disturbance giving ages at around 1.4-1.5 Ga was recently identified in the Re-Os of bulk sample fractions of NWA 7034 (Goderis et al., 2016).

2.2. Pyrite

Pyrite (<1.0 vol.%) occurs as cubes, truncated cubes and octahedra (average grain size 30-40 μm) in each lithology of the meteorite, from the Pre-Noachian lithic clasts to late veins postdating the 1.4 Ga-old annealing and lithification event of the fine-grained matrix (Lorand et al., 2015). Cubic crystals were observed mostly inside open cracks, low-Ca pyroxene clots and ICM. These crystals are inferred to have crystallized after the final assembly of the breccia at T < 400-500°C from its maximum Ni content (up to 4.5 wt.%; EMPA and SEM EDS/EDX data). The few highly resorbed pyrrhotite relicts coexisting with the pyrite indicate near neutral H_2S-HS-rich hydrothermal fluids (6<pH<10), at minimum log fO_2 of > FMQ + 2 log units (Lorand et al., 2015; Wittmann et al., 2015). Several pyrite-producing sulfidation reactions took place, involving either magnetite/maghemite, the low-Ca pyroxene, or direct precipitation of dissolved divalent iron. Many pyrite grains have trapped the fine dust of iron oxides (micron-sized Fe-(Ti) oxides identified as magnetite-maghemite; Agee et al., 2013) that are so abundant in NWA 7533 (Hewins et al. 2017).

All pyrite grains show fracture networks which result from the weak shock event that liberated the meteorite from the Martian subsurface crust. These fractures acted as preferential pathways for partial replacement of pyrite by iron oxyhydroxides of terrestrial origin, as suggested by their D/H values and their distribution defining an alteration gradient through the meteorite (Lorand et al., 2015). The net effect of this alteration was to remove most of the S originally present as pyrite. The sharp difference between the bulk-rock S analysis (820 ppm; Humayun et al., 2013) and the theoretical S content that can be deduced from pyrite modal abundances (up to 5,400 ppm) indicates that terrestrial alteration may have leached up to 80% of the initial S budget. Meteorites that experienced such hot desert alteration generally display similar S losses (e.g., Dreibus et al. 1995).

3. ANALYTICAL METHODS.

Three polished sections were studied (NWA 7533-5 and NWA 7533-7 at Université de Nantes and NWA 7533-3 at Florida State University). NWA 7533-5 contains the least altered pyrites (15 of the 23 crystals analyzed are less than 50% altered; see Fig. 1 in Lorand et al., 2015). Their major (Fe, Ni, S) and minor element (Co, Zn, Cu, As, Se) compositions (Camparis SXFive Cameca EMP) were documented in Lorand et al (2015). NWA 7533-7 is a new thick section made for the purpose of this study. Its pyrite modal abundance (1 vol.%; determined by point counting on 9000 points at 50 micron steps) fits well the range published for the other sections. NWA 7533-7 pyrites were studied with a Tescan VEGA II LSU Scanning Electron Microscope (SEM) operating in conventional (high-vacuum) mode, and equipped with an SD3 (Bruker) EDS detector (Muséum National d'Histoire Naturelle Paris, France, MNHN). Major element concentrations (Fe, Ni, Co, S) were determined at 15 kV accelerating voltage with a PhiRoZ EDS standardless procedure. Lorand et al. (2015) provided comparison between SEM-EDX and EMP analyses of NWA 7533 pyrites, demonstrating that such a procedure can produce reliable data for major element compositions of pyrite.

Chalcophile-siderophile trace element concentrations were obtained in-situ using an LA-ICP-MS at the «Laboratoire de Planétologie et Géodynamique à Nantes». The samples were ablated and elements collected using a Photon Machine Analyte G2 equipped with an excimer laser (193 nm laser wavelength) and a dual volume sample cell that keeps the sample volume small and constant. Most analyses were performed with a repetition rate of 10 Hz in spot mode using a laser output energy of 90 mJ with a 50% attenuator and 20x demagnification, resulting in low fluences on the sample (<4 J/m^2), to minimize pyrite melting and attendant trace-element fractionation (e.g. Wohlgemuth-Ueberwasser et al., 2007). The ablated sample material was transported in a mixture of H-He-Ar through a cross-flow nebulizer to a Varian 880 quadrupole ICP-MS. Given the small fine grain size and scarcity of sulfide grains suitable in size for LA-ICP-MS analysis, spot sizes for standards and samples were set to 25 μm for small grains, and one to three spots per grain were analyzed, depending on grain size. Only the largest crystals (>30 microns; preserving unaltered core zones) were suitable for laser ablation analyses of pure pyrite. Smaller spot sizes (down to 10 μm) were used on particularly fine-grained pyrite isolated within Fe oxyhydroxides or Fe (Ti) oxides. These mixed (pyrite + Fe (Ti) oxide or pyrite + Fe oxyhydroxides) grains analyzed are hereafter referred to as mixes. A total of 84 spot analyses were conducted on 52 pyrite grains (Table S1).

The following isotopes were collected ^{29}Si, ^{34}S, ^{51}V, ^{57}Fe, ^{59}Co, ^{60}Ni, ^{61}Ni, ^{63}Cu, ^{65}Cu, ^{66}Zn, ^{75}As, ^{77}Se, ^{95}Mo, ^{99}Ru, ^{102}Ru, ^{103}Rh, ^{105}Pd, ^{106}Pd, ^{107}Ag, ^{108}Pd, ^{118}Sn, ^{120}Sn, ^{121}Sb, ^{125}Te, ^{126}Te, ^{189}Os, ^{190}Os, ^{191}Ir, ^{193}Ir, ^{194}Pt, ^{195}Pt, ^{197}Au, ^{202}Hg, ^{205}Tl, ^{207}Pb, ^{208}Pb and ^{209}Bi). Possible contamination from matrix silicates or Fe oxides or

oxyhydroxides were detected by monitoring signals for Si and Fe. Isotopes of each element to be analyzed, length of analysis (for spots) and dwell time were set to minimize potential interferences and maximize counting statistics – with overall mass sweep time kept to ~1 s. Major elements (S, Fe) were counted in the low-count rate mode to avoid saturation of detectors. Synthetic sulfides (i.e., NiS_2 and $CuFeS_2$) devoid of PGE (< ppb concentration levels) were analyzed for evaluating mass interference corrections between Ni- as well as Cu-argides ($^{62}Ni^{40}Ar$, $^{63}Cu^{40}Ar$ and $^{65}Cu^{40}Ar$) and the isotopes ^{102}Ru, ^{103}Rh and ^{105}Pd used for the element quantifications. No significant interference was observed. There is no correlation between Rh and Cu concentrations that are very low (< 104 ppm) in NWA 7533 pyrite (Table S1). The interference of $^{59}Co^{40}Ar$ on ^{99}Ru was also negligible.

Data were acquired in four 8-hours separate analytical sessions over an interval of one year. In each analysis, the gas blank (laser off) was collected for 30/40 s prior and after laser ablation. Each ablation run was analyzed in detail in time-integrated count diagrams to retrieve any metal-rich microparticles not residing inside the pyrite. In practice, due to the small area of unaltered pyrite available, a few tens of seconds were available for extracting elemental concentrations of pyrite before contamination from Fe oxides/hydroxides or surrounding silicates increased Si, Ga, Fe and V concentrations. Data reduction was done using Glitter™ software (Griffin et al., 2008). External calibration was performed with synthetic standards MASS-1 (pressed Zn sulfide powder; Wilson et al., 2002), NIST-610 and an in-house synthetic PGE-doped NiS (SARM-7 10) which is a 7.5 g fused nickel sulfide doped with 15 g of South African rock standard SARM-7 (Lorand et al., 2010). Both standards were compared with published values to confirm homogeneity of standards with respect to elements of interest and proved to be well within error. Each standard was analyzed twice every ten analyses to bracket sample measurements at the beginning and at the end of a single ablation run to reduce the effects of possible standard heterogeneity. Analyses of pyrite were quantified with S as internal standard, using S concentration measured by EMPA (Lorand et al., 2015). Analyses of mixes starting in pyrite and ending in Fe oxyhydroxides were quantified with S and Fe as internal standard assuming that EMPA data of pure phases apply (Lorand et al., 2015; Hewins et al., 2017) and linear mixing between pyrite and Fe-oxyhydroxides, the pyrite/Fe oxyhydroxide ratio being calculated from Fe/S count rates in time-integrated count diagrams. Of course, these metal concentration data are to be considered as semi-quantitative although they should not alter correlations in binary plots between metals. The detection limits in each quantification were calculated for each analysis from the gas blank and the sensitivity of the reference materials following the equations in Longerich et al. (1996).

The full results of LA-ICP-MS analyses including standard deviation and limit of detection for each analysis are listed in Table S1; correlation coefficients for element pairs are given in Table

S2. The accuracy of analyses of external standards measured as unknowns (SARM-7 10 and MASS-1) was good for Os, Ir, Pt, Pd and Au (<10% relative difference to certified/theoretical values) (supplementary Tables S3 and S4). Analytical reproducibility was monitored by the repeated analysis of the sulfide standard MASS-1 yielding 5% relative standard deviation (RSD) for all elements (supplementary Table S4). In addition to pyrite, four crystals totally replaced by Fe oxyhydroxides and one grain of Fe-Ti oxide were analyzed with MASS-1 and NIST 610 as external standard and Fe as internal standards (EMPA data: Lorand et al 2015; Hewins et al., 2017).

In addition to spot analyses of pyrite, chalcophile-siderophile trace elements were also analyzed on the matrix of NWA 7533-3 using an Electro Scientific Industries New Wave™ UP193FX excimer laser ablation system coupled to a Thermo Element XR™ magnetic sector ICP-MS at Florida State University (Humayun et al., 2013). Pyrite (or mixed pyrite-matrix) composition was investigated by running a 2,000 μm line scan along the length of a CLMR clast (Clast XIV) with a 20 μm spot size, at 5 μm/s, with 50 Hz repetition rate and examining the data in time-resolved mode. The mass spectrum was swept repeatedly for the intensities of 60 elements (Yang et al., 2015). Detection limits were estimated conservatively using the 3-sigma variation of 12 blanks taken before and after the analysis, and standardization followed Yang et al. (2015).

4. RESULTS

Results for the transect through the CLMR clast (XIV) are shown in Fig. 1. The line scan intersected 2 larger pyrite grains and about 5 smaller ones. The abundances of Se and Te roughly correlate in the pyrites (as do Pb, Co and Ni). However, the correlation with S is weak because each ablated pyrite experienced a different degree of terrestrial oxidation and S loss (Lorand et al., 2015), in addition to being variably enriched in Se and Te (see below). Distance-integrated count diagrams produced transient concentration spikes for several HSE. Such transient spikes are usually interpreted as reflecting occurrence of HSE-rich micronuggets in the ablated area (Lorand et al., 2008; 2010; Lorand and Luguet, 2016; O'Driscoll et al., 2016). These are Ru-, Pt- or Os-rich micronuggets, not necessarily located inside the pyrite, as shown by the decoupling between S, Se or Te peaks and HSE spikes: the largest micronugget (a Ru+Ir grain with subchondritic levels of Rh, Os and Pt) was probably pasted (i.e. not fully enclosed) on a pyrite crystal because the corresponding HSE concentration peaks are clearly offset from the S peak in Fig. 1.

Spot analyses of pyrite and mixes produced a wide range of trace element concentrations for chalcophile-siderophile elements, from sub-ppm levels to hundreds of ppm, except Ni and Co, that reach major and minor element concentrations respectively, as expected from previous EMP and SEM-EDX analyses. For convenience, the results will be discussed by sorting the analyzed

elements from the highly siderophile, most refractory elements (HSE) to the most volatile chalcophiles.

4.1 Highly siderophile elements.

As observed in the transect through clast XIV, time-integrated count diagrams of pyrite analyses produced transient concentration spikes for each of the six platinum-group element (PGE = Os, Ir, Ru, Rh, Pt and Pd) in about half of the analysed pyrite (Fig. 2). Previous SEM detections in NWA 7533 pyrite supports this widespread occurrence of HSE micronuggets (Lorand et al., 2015). Up to 3 micronuggets were detected in a single analysis, displaying various combinations between Os, Ir, Ru, Pt and Rh (Fig. 2). Rhenium was detected in one nugget that combines Os-Ir-Re-Mo-Pt-Rh (Fig. 2). The size of each nugget (estimated with Longerich et al. (1996) formulas relating the average volume ablated by time unit to the analytical conditions) is estimated to range between one micrometer or less, to 4-5 μm for the largest one (assuming spherical micronuggets). Palladium is not associated with refractory PGEs, being found to occur alone or occasionally with Au peaks (four micronuggets). However, such Pd spikes could be analytical artifact because they show very low (< 10) peak/background ratio.

Calculated HSE concentrations range between 0.01 and 0.6 ppm, apart from Ru that shows on average higher mean values (up to 4 ppm; Table S1). Although half of their concentrations were below detection limits, Os, Ir and Pt produce positive correlations in binary plots (R^2 = 0.62 for Os vs. Ir, 0.70 for Pt vs. Ir and 0.56 for Pt vs. Os respectively; Table S2) (Fig. 3A), if pure pyrite analyses are taken into account. Platinum/iridium and Pt/Os ratios are close to chondritic, without a clear match to any specific chondrite class. All of the analyzed pyrites are Mo-enriched relative to chondritic ratios although some analyses define a positive correlation between Mo and Pt (R^2 = 0.74; Table S2) (Fig. 3B). The Re vs Os plot (not shown) shows virtually no correlation and a wide range of Re/Os ratios (from Re/Os = 0 to Re/Os>10). Rhenium correlates neither with Mo nor with any other element in the pyrites, except Pt (R^2 = 0.51, pyrite analyses only). It is worth noting that these correlations are strongly biased by a few HSE-rich outliers likely corresponding to HSE-rich micronuggets integrated in the quantification (e.g. 7533-5-20; 7533-7-9).

As suggested by the decoupling between Pd-dominated and Pt-dominated HSE micronuggets, there is virtually no correlation between Pd and Pt (R^2= 0.13), nor between Pd and Ru or Rh. Likewise, the correlation between Ru and Ir is poor (R^2= 0.26) (Table S2).

4.2 Moderately siderophiles Ni, Co, Ag, Au, Cu

LA-ICP-MS data strongly support previous EMPA and SEM-EDX analyses of Lorand et al. (2015) in showing that NWA 7533 pyrite are Ni- and Co-enriched (156<Ni<23,417 ppm Ni;

57.8<Co<568 ppm). A few EMP analyses defined a loosely constant Ni/Co around 10, reminiscent of meteoritic metal compositions: the new LA-ICP-MS analyses produce a more robust correlation between Ni and Co (R^2 = 0.72; Table S2); their Ni/Co ratios (10 to 20) are close to those of chondritic nickel-iron alloys (Fig. 4). This correlation is not significantly degraded if mixes (pyrite + Fe oxyhydroxides) are taken into account. Few analyses show Ni/Co >20, reflecting Ni-enrichment. As shown in Lorand et al (2015), the high-Ni pyrite occurs as irregularly shaped, discontinuous areas that are randomly distributed inside a single pyrite crystal. Such areas may not be adequately sampled by the laser beam during LA-ICPMS analyses.

Gold does not show any specific correlation with Ag and Cu, or with the other elements analyzed in NWA 7533 pyrite, apart perhaps with Pd (R^2 = 0.56), in agreement with the few Au-Pd micronuggets detected in time-integrated LA-ICPMS diagrams. Silver concentrations (0.01-1 ppm) are similar to Au concentrations (0.01-0.7 ppm); however Ag/Au ratios (0.4-25) are higher than chondritic (0.5-1.25; Wasson and Kallemeyn, 1988; Tagle and Berlin, 2008; Fisher-Gödde et al. 2010).

LA-ICPMS Cu data (12.7-104 ppm) are consistent with previous EMP analyses that did not detect Cu (<91 ppm). Copper does not correlate with Ni, Co, or Zn (Table S2). Copper is severely depleted with respect to Ag (0.0015<Ag/Cu<0.05) when compared with chondrite compositions (0.0015<Ag/Cu<0.0007; Wasson and Kallemeyn, 1988; Tagle and Berlin, 2008; Fisher-Gödde et al. 2010).

4.3 Volatile chalcogen and semi-metals Se, Te, As, Sb, Bi

Selenium concentrations range between 8.8 and 149 ppm, and those of Te between 4.4 and 104 ppm, respectively, excluding a few Te-rich outliers (up to 262 ppm, Table S1). As suggested by EMP analyses on 7533-5 pyrites (Lorand et al., 2015), Se and Ni correlate positively (R^2 = 0.71) as do Co and Se (R^2 = 0.60), regardless of whether the grains analyzed were pure pyrite or mixes. However, the curve in Fig. 5 extends down to much lower Se concentrations compared to EMPA because LA- ICPMS analyses have much better limits of detection (down to 10 ppm vs. 64 ppm). Taken as a whole, Se/Ni ratios are superchondritic (>0.06 vs 0.01) as are S/Se ratios (3,300-54,000 vs. 2,560+/-200; Dreibus et al., 1995; Palme and O'Neill, 2014).

Tellurium also positively correlates with Se while being strongly enriched with respect to chondritic Se/Te ratios. However, the correlation in Fig. 5B is much weaker (R^2 = 0.16; Table S2) because several Te-enriched outliers corresponding to both analyses of pyrite and mixes have extreme Te/Se ratios (4 to 10). Three outliers (all corresponding to mix analyses) also stand out by coupled concentration ranges (e.g. 7533.5-24; 7533.7-20; Fig. 6; Table S1). Such Te-Bi-Pb-rich

areas may correspond to telluride microinclusions although corresponding concentration spikes are lacking in the time-resolved LA-ICP-MS spectra of these grains.

Arsenic concentrations (2.5-32.3 ppm) are well below the limit of detection (117 ppm) of previous EMP analyses reported by Lorand et al. (2015). Antimony is even more depleted (0.02-0.30 ppm) as is Bi (0.11-1.8 ppm). Correlations between Se and As or Sb vs. As are lacking (Table S2). Some mixes that incorporated major amounts of Fe oxyhydroxides (7533-7-36 to 7533-7-40) are enriched in As and Sb by a factor 2 to 5 compared to pyrite (5.7-30 ppm; Table S1).

4.4 Volatile chalcophiles Pb, Hg, In, Tl

Lead (2-70.0 ppm) positively correlates with Te (R^2 = 0.66) and Bi (R^2 = 0.62; Fig. 6). These correlations are significantly poorer if the mixes are taken into account owing to their larger range of Bi and Pb concentrations. No noticeable covariation trend between Tl (0.02-0.65 ppm), Hg (0.003-0.6 ppm) and In (0.008-0.13 ppm) or between one of these elements and the other elements analyzed here can be detected (Table 2).

4.5 Moderately chalcophiles Sn, Zn, Ga, V

These four elements that also have lithophile properties (e.g. Palme and O'Neill, 2004) produce a series of rather good positive correlations between Ga and V (R^2= 0.8), Sn and V (R^2= 0.63), Ga and Sn (R^2 = 0.59) and Ga and Zn (R^2= 0.58; Table S2). The V- and Ga-rich end-member in the V vs. Ga plot of Fig. 7A is the only Fe-Ti oxide so far analyzed (40 ppm Ga, 460-500 ppm Zn and 300 ppm V). Thus, the trend in Fig. 7A is probably a mixing trend between pyrite and iron-titanium oxides resulting from beam overlap. The regression line in Fig. 7A intercepts the x- and -y axes at very low V (<50 ppm) and Ga contents (<2 ppm) that may represent the actual amount inside pyrite. Zinc also positively correlates with V; however most of the pyrite analyses show variable Zn contents (10-140 ppm) for a narrow V concentration range (Fig. 7B).

5. DISCUSSION

5.1 Mass balance calculation of the contribution of pyrite.

Because no data base is available for martian pyrite, any comparison must be made with terrestrial samples. Compared to terrestrial pyrites of hydrothermal origin, NWA 7533 pyrites are enriched in Ni and Co, and on average depleted in all of the chalcophile-siderophiles including gold, silver, copper and semi-metals except selenium and tellurium as well as all fluid-mobile volatile elements (Hg, Tl, In; Fig. 8). This conclusion also pertains to HSE, especially Ru, Ir and Os that are the most soluble HSE in pyrite (up to 470 ppm Ru and 390 ppm Ir; e.g. Dare et al., 2011; Lorand et al., 2011; Pina et al., 2015; not shown in Fig. 8).

Pyrite is by far the most abundant hydrothermal sulfide and no other major S-bearing mineral has been identified in the NWA 7533/7034/7455 paired meteorites. Before discussing the origin of its chalcophile-siderophile element budget, it is interesting to estimate the contribution of pyrite to the whole-rock budget first. Details of the mass balance calculation, which combines the bulk analyses of NWA 7533 lithological units, the pyrite modal abundances and the in-situ analyses of unaltered pyrite grains only, are given in supplementary Table S5. Fig. 9 shows that pyrite is a minor contributor for all elements but the chalcogens Se and Te (50-70%) in addition to S. The contribution of some elements (Mo, Ru, Ni, Au, As and Ag) may be underestimated, owing to their large concentration range. It is worth noting that all of these elements are known to enter the pyrite crystal lattice, Se (and Te) by replacing S^{2-} in the anionic sublattice of pyrite, divalent Co and Ni (like Os^{2+} and Ru^{2+} that have ionic radii quite similar to those of Fe^{2+}) replacing Fe by stoichiometric substitution (e.g. Vaughan and Craig, 1997; Abraitis et al., 2004; Lorand and Alard, 2011; Pina et al., 2013). Gold has been found to enter pyrite by coupled substitution with As (Reich et al., 2005; Deditius et al, 2014). Pyrite accounts for <10% of the bulk-rock budget of all other analyzed elements, especially the weakly chalcophiles (Zn, Sn, V, Ga) and the volatile chalcophiles (Hg, In, Cd, Tl).

Of course, the whole-rock budget of HSE is assumed to be balanced by HSE-rich micronuggets that occur outside pyrite (e.g. Fig. 1). Major hosts for Ni and Co are mafic silicates (low-Ca and high-Ca pyroxenes which represent more than 43 % by volume of the impact breccia (Agee et al., 2013), chromite, Fe-(Ti) oxides, (up to 0.3-0.4 wt% NiO in Ti- and Cr- magnetite; Hewins et al., 2014a; 2017) (see also Table S1). Regarding Cu, Zn, Pb, no discrete (sulfide?) minerals were discovered, despite careful SEM investigations on eight polished thin sections. Lead has been suggested to be partitioned between apatite, feldspar, zircon and other minor minerals (Humayun et al., 2013; Belluci et al., 2015). The most significant contributors for Pb, Zn, V, Ga, In, and Sn are Fe-Ti oxides in addition to chromite (Zn, V), low-Ca and high-Ca pyroxenes and apatite (V). Our LA-ICP-MS analysis (Table S1) coupled with the modal proportions of Fe-Ti oxides reported by Agee et al. (2013) for NWA 7034 (9.7+/-2.6 wt.%) indicate that Fe-Ti oxides can balance half of the whole-rock budget of NWA 7533 for V, Zn, and Ga. Magnetite can also accommodate Ru, Rh and Ir in its 'divalent' octahedral sites (Capobianco and Drake, 1994; Pagé et al., 2012; Brenan et al., 2016). The only analysis of Fe-Ti oxide available is Rh-enriched compared to pure pyrite (>0.1 ppm) as are several analyses of mixes that may have incorporated Fe-Ti oxides (Table S1).

The four Fe-oxyhydroxide crystals analyzed are strongly depleted in S compared to pure pyrite (3,900-5,000 vs. 54,000 ppm; Table S1); their S/Se ratios (137-1,193) are one order of magnitude lower than those of unaltered pyrite (3,350-54,000) thus supporting the huge S loss that

occurred during terrestrial weathering. By contrast, the four analyzed crystals do not show indisputable evidence of enrichment/depletion trends in their chalcophile/siderophile element systematics compared to pyrite, even for highly volatile elements such as Tl and Hg. Only the fluid-mobile elements Pb, Sb, Bi and As show evidence of scattered distribution toward depletion (Pb) or enrichment (As) **(**Table S1).

5.2 Early impactor(s)-derived HSE material inside pyrite.

There is a consensus for considering the siderophile element budget (HSE, Ni, Co) of martian regolith impact breccias NWA 7034 and paired samples as impactor materials from the early bombardment of the ancient martian crust, accumulated more than 4.3 Ga ago (Humayun et al., 2013; Wittmann et al., 2015; Goderis et al., 2016). Goderis et al (2016) found weighted mean whole-rock HSE contents for NWA 7034 corresponding to 3 wt. % of chondritic impactor material (isotope dilution-ID-ICP-MS analyses). In line with Lorand et al. (2015), one may therefore assume that the HSE-rich micronugget inclusions in NWA 7533 pyrite are impactor materials that were trapped by pyrite. These HSE micronuggets actually occur indiscriminately in pyrite, altered pyrite, and outside the pyrite, which supports the idea of random trapping by pyrite. This occurred ca 3 B.Y. after the early bombardment if we accept that pyrite is one of the latest minerals in the Martian chronology of NWA 7533, crystallized during the 1.4 Ga lithification and annealing events (McCubbin et al., 2016; Hewins et al., 2017). However there is no evidence that such micronuggets served as nucleation sites for pyrite because they were not identified in all of the pyrite crystals analyzed by LA-ICP-MS.

Compared to partial SEM analyses reported by Lorand et al (2015), LA-ICP-MS analyses indicate a much wider compositional range combining mainly refractory PGE (Os, Ir, Ru, Rh, Pt) with Mo and Re. Such alloy compositions are known only in refractory metal nuggets (RMN) from carbonaceous chondrites and unknown as magmatic and hydrothermal platinum-group minerals (Cabri, 1981; O'Drisscoll and Gonzales-Jimenez, 2016 and references therein). RMN are interpreted as early condensates of Calcium Aluminium inclusions (Palme and Wlotska, 1976; Harries et al., 2012; Hewins et al. 2014b). However, the micronuggets identified in NWA 7533 pyrites are highly fractionated and not exactly rich in all of the refractory siderophiles (especially Mo and Re) seen in carbonaceous chondrites studied so far. Moreover, HSE nuggets are not found in some CAIs (e.g. in Efremovka or Leoville) where HSEs are dissolved in Fe-Ni alloy (e.g., Campbell et al., 2003). The more likely scenario, given that most of the original mineralogy of the breccia, including impactor components, has been erased by pre-Noachian alteration, is that the micronuggets probably formed or were modified by weathering and impact melting prior to the assembly of the breccia. The large range of micronugget compositions detected by LA-ICP-MS accounts for significant deviations

from chondritic patterns measured for many whole-rock subsamples of NWA 7034 that cannot be accounted for by the respective analytical uncertainties (Goderis et al., 2016). Goderis et al. (2016) pointed out that such deviations definitely preclude reliable identification of projectile components from whole-rock analyses, inasmuch as multiple impactor components were probably admixed during regolith formation (Humayun et al., 2013). The same is also true for pyrite-hosted HSE micronuggets.

In addition to early Noachian alteration in the martian regolith, HSE micronuggets were also variably reprocessed within pyrite. The high (up to 2-4 ppm) Ru contents of some pyrite that are independent of concentration spikes in time-resolved diagrams can be explained by such reequilibration with Ru-bearing HSE micronuggets. Time to reequilibrate pyrite at 400°C is quite short (about 100 years; Barton, 1970). By contrast, Os shows stronger preference for Pt-Ir-(Os) alloys (Cabri et al., 1996; Lorand et al., 2010; O'Driscoll and Gonzales-Jimenez, 2016 and references therein). It requires higher fugacity of S compared to Ru to occur as sulfides and the uptake of Os in pyrite only occurs when grain growth occurs because the diffusion of Os in pyrite is limited to near the surface (Brenan and Rose, 2000). One may surmise that such decoupled behaviour between Ru and Os is responsible for the poor correlation coefficient of the Ru vs. Os plot (e.g. Table S2).

In contrast to HSE, Ni and Co produce smooth signals in time-integrated LA-ICPMS diagrams which rule out occurrences of Fe-Ni alloy micronuggets at the submicron scale. This observation provides further support to the Lorand et al (2015) suggestion that meteoritic Fe-Ni metal was likely oxidized into Fe-(Ti) oxides well before pyrite formation, which then served as the Fe-Ni-Co reservoir for pyrite crystallization. The wide range of Ni-Co concentrations revealed by LA-ICPMS analyses is therefore consistent with occasional contamination of growing pyrite crystals by such oxides, followed by diffusion of Ni and Co inside the pyrite.

5.3 Input of hydrothermal fluids to NWA 7533 pyrite.

At first sight, siderophile-chalcophile metal contents occur in NWA 7533 pyrite as trace concentration levels far from the saturation threshold suggested by terrestrial hydrothermal pyrites in Fig. 9. Apart from the most siderophile elements (PGE, Re, Au) that were likely recycled from early impactor materials predating pyrite, all the other chalcophile-siderophile elements are assumed to be now in solid solution inside pyrite. They were most probably delivered by the fluid pulse(s) that precipitated pyrite during the 1.4 Ga-old hydrothermal event. As said before, pyrite controls the bulk-rock budget of only three elements: the chalcogens (Se, Te; Fig. 9), along with S (not shown). It is worth recalling that martian impact breccias are conspicuously poor in magmatic sulfides, i.e. po-pn (Cu) sulfides assemblages crystallized from sulfide melts as documented for

example in SNC meteorites (e.g. Baumgarnter et al., 2017; Lorand et al., 2018). Lorand et al. (2015) detected only two tiny (<10 μm across) sulfide blebs of Ni-rich pyrrhotite + pentlandite enclosed in plagioclase clasts in the 8 polished thin sections studied. The reason for this depletion is probably twofold (1) The heavy bombardment by chondritic meteorite material may have degassed S, a volatile element. Nickel was demonstrated to behave as a lithophile element in the crystallization sequence of impact-melt derived monzonitic clasts, which means that the impact melt was S-undersaturated (Hewins et al., 2014a). (2) The brecciated crust underwent early Noachian weathering and oxidation producing abundant Fe^{3+}-rich oxides (magnetite/maghemite; Nemchin et al., 2014; Humayun et al., 2014). These conditions would have also oxidized any relict of magmatic Fe-Ni-Cu sulfides not enclosed within silicates into sulfates. Regardless of which (not mutually exclusive) interpretation holds true, it is pyrite, the only major S mineral found in NWA 7533 (Hewins et al., 2017) that rejuvenated the S budget of martian regolith breccias.

The same is also true for Se and Te that are strongly tied to S chemistry. All three elements are transported as H_2S, H_2Se and H_2Te in reduced hydrothermal fluids (Grundler et al., 2013). Although within the accepted range for hydrothermal sulfides (Huston et al. 1995; Luguet et al. 2004; Lorand and Luguet, 2016 and references therein), S/Se ratios vary within a factor of 15 (3,375–54,000), mainly because of the highly variable Se concentrations in NWA 7533 pyrite (8.8-149 ppm). Sulfur and selenium can be fractionated from each other by hydrothermal fluids within a narrow window of redox conditions above FMQ because sulfur dioxide coexists with elemental Se (Huston et al., 1995; Lorand et al., 2003 and reference therein). Temperature also plays a major role in the incorporation of Se and Te in the anionic sublattice of the pyrite structure (Maslennikov et al., 2009; Wohlgemuth-Ueberwasser et al., 2015; Keith et al., 2016). Studies of fossil and active hydrothermal systems revealed that Se-rich pyrites are high temperature pyrite precipitates (Auclair et al., 1987; Maslennikov et al., 2009; Genna and Gaboury, 2015). Selenides form at higher T than corresponding sulfides and high-T sulfides show higher Se contents (Keith et al., 2016). Since Ni concentrations in pyrite also show the same positive temperature-dependence (e.g. Abraitis et al., 2004), the Se vs Ni positive correlation of Fig. 5 is assumed to result from crystallization of NWA 7533 pyrite over a wide temperature range (from 500°C to unknown value; Lorand et al., 2015).

In addition to superchondritic S/Se ratios, NWA 7533 pyrites display superchondritic Te/Se that is not expected because tellurium is less chalcophile than Se and preferential uptake of Te by the pyrite lattice is counterintuitive. As a semi-metal, Te shows more metallic behavior (e.g. Brenan et al., 2016 and references therein). It is commonly found as metal tellurides and as native tellurium (e.g., Te(0)) in magmatic and hydrothermal ore deposits (e.g. Cook et al., 2007; Voudouris et al, 2011); tellurides are stable over a wider fO2 range (below the magnetite–hematite buffer) compared to sulfides and selenides and the stability of native tellurium overlaps the magnetite–hematite buffer

(e.g., Grundler et al., 2013; Schirmer et al., 2014). Thus, during martian oxidation, one would expect preferential uptake of Te in the oxidized source and less availability of this element for S-rich fluids. The fact that NWA 7533 pyrite exhibits superchondritic Te/Se may result from precipitation of Bi-Pb-Te tellurides or intermetallic compounds at the interface between pyrite and hydrothermal fluid. This interpretation is supported by rather good positive correlations in the Te vs. Bi and Te vs. Pb plots of Fig. 6 for unaltered pyrite as well as Pb-,Te- and Bi-enriched outliers.

We may also speculate that the hydrothermal fluids tapped a pre-enriched Te source resulting from accumulation of chondritic impactor-derived Fe-Ni metals. While the purely chalcophile element Se is exclusively hosted in sulfides (e. g. Dreibus et al. 1995; Lorand and Luguet, 2016; Baumgartner et al., 2017), the partly siderophile element Te can also be incorporated in the metal phases in chondritic meteorites (Funk et al., 2015). In CK and R chondrites and refractory inclusions in CV chondrites, Te additionally forms noble metal-rich tellurides such as chengbolite ($PtTe_2$) and moncheite ($PtTe_2$). Accreted Fe-Ni metal degraded by oxidizing fluids may be an extraneous supply of Te that was then recycled as reduced tellurides by hydrothermal fluids. Of course, this interpretation is consistent with the theory of telluride precipitation discussed above.

The typically euhedral crystals (cubooctahedra, with no framboids, no colloform growths) of NWA 7533 pyrite suggest that its depositional process was near equilibrium, under a low degree of supersaturation in the fluids (Murowchick and Barnes, 1986; Keith et al, 2016). Rapid precipitation in high-gradient zones generates strong zoning that are lacking in NWA 7533 pyrite crystals (Vaughan and Craig, 1997; Patten et al., 2016; Duran et al., 2015). The chalcophile element depletion of NWA 7533 pyrite cannot therefore be explained by disequilibrium partitioning processes. We may also speculate that the current compositions of pyrite potentially equilibrated with different hydrothermal fluid(s) but this alternative remains difficult to address without systematic age determinations on pyrite that are presently lacking. Our discussion will be focused on three points i) physical conditions (temperature) of partitioning between hydrothermal fluid(s) and pyrite, ii) nature and composition (redox) of hydrothermal fluids, iii) the availability of these elements in the pre-Noachian crust sampled by martian impact breccias.

Clearly, one central reason for the chalcophile metal-depleted composition of NWA 7533 pyrite may be the lack of precursor magmatic sulfides in the heavily impacted Noachian crust sampled by NWA 7533. On Earth, metal-rich hydrothermal ore deposits generally have ore sources located in magmatic rocks that host base metal sulfides (Cu-Fe-Ni sulfides). Leaching of magmatic sulfides under high-temperature greenschist facies conditions is considered to be an important source of metals (Au, Cu, Pb, Ag, Ni, Au, As, Sb, Te) while silicate alteration can release Zn, As, Mo, Sb from Fe-Ti oxides (Kaassalinen et al 2015; Hannington et al, 1990; Patten et al, 2016 and references therein).

583 The compositional and textural features of pyrite are closely related to the temperature and
584 chemical characteristics of its host environment (Abraitis et al., 2004). Changing temperature
585 affects the solubility of many minerals in hydrothermal fluids (Seyfried and Ding, 1995, Wilkin and
586 Barnes 1997; Findlay et al 2015). Selenium, Bi, Sn, Mo, Te, and Co, are low solubility elements
587 that precipitate at high T (>350°C) in terrestrial active hydrothermal vents (Maslennikov et al.,
588 2009). By contrast, chalcophile metals (Au, Ag, As, Sb, Pb, Zn, Cd, Hg, Tl, Ga) are associated with
589 lower T pyrite (<350°C; e.g. Hannington et al, 1991). Thallium, a high solubility element in
590 hydrothermal fluids, is concentrated (up to 10,000 ppm) in low-T (100-250°C) pyrite and marcasite
591 deposition within the outer walls of hydrothermal chimneys (Smith and Carson, 1977; Sobbot et al.,
592 1987). The chalcophile element systematics of NWA 7533 pyrite is therefore perfectly consistent
593 with the high crystallization temperature deduced from Ni and Se contents.
594 It is well known that speciation of such metals in hydrothermal fluids strongly depends on
595 fluid composition, especially on ligands and pH. Solubility values can be estimated for several
596 elements (Cu, Pb, Zn, Au). Sulfur and chlorine are the two most important ligands accounting for
597 metal transport in hydrothermal fluids (Helgeson, 1970; Barnes, 1979; 2015; Kaassalinen et al.,
598 2015). According to Fig. 10A, the assemblage pyrite-magnetite-hematite for FMQ + 2 log units
599 corresponds to near neutral fluids (pH = 6-7) in equilibrium with pyrite-magnetite-hematite at
600 350°C. Such fluids are expected to contain a moderate amount of H_2S with all metals including Cu,
601 Pb and Zn delivered as hydrosulfides. Numerical modelling by Zhong et al (2015) suggests that
602 low-salinity hydrous fluids (<3wt.% NaCl) in equilibrium with magnetite-pyrite-hematite at 400°C
603 can dissolve 1 to 100 ppm Cu, Pb and Zn, whereas the experiments of Gibert et al. (1998) indicate
604 0.1 ppm Au as $Au(HS)^{2-}$ (Fig. 10B). These concentration ranges measured in synthetic fluids are
605 very similar to those measured in NWA 7533 pyrites. Unless unrealistically low pyrite-fluid
606 partition coefficients close to 1 are assumed, we may conclude that fluids that precipitated NWA
607 7533 pyrite did not reach saturation for these four elements.
608 As high-valence, small ions, Zn and Pb can be more readily complexed with Cl^- over a wide
609 range of T and acidic conditions (Zhong et al, 2015). Chlorine-bearing fluids may have been present
610 at some stage of the 1.4 Ga-old sequence of hydrothermal alteration in NWA 7533: apatite is a
611 major Cl-rich mineral (up to 7.2 wt.%) in NWA 7533 (Hewins et al., 2017). Belluci et al (2017)
612 documented a core-rim increase of Cl/F ratios coupled with some fractionation in Cl isotopic
613 compositions in matrix apatite, compared to original magmatic $\delta^{37}Cl$ signatures. One may surmise
614 that apatite continued to re-equilibrate with fluids down to temperatures of 500°C and buffered the
615 fluid composition to near zero Cl contents, thus reducing metal-chloride complexing. Except for a
616 few smectites of uncertain origin (Muttik et al., 2014), NWA 7533 silicate assemblages are
617 remarkably immune to acid leaching that typically generates microcrystalline silica, kaolinite,

pyrite, barite and sericite (see Einaudi et al., 2003; Scher et al., 2013). Potassium-rich feldspar does not show evidence of alteration to kaolinite, not even incipient sericitization, which is expected for highly saline acidic fluids at pH <6 (Fig. 10).

6. Conclusions

Pyrite accounts for more than 50-70 (+/- 20) % of the bulk rock budget for Se and Te (and probably for S too before terrestrial weathering). It displays superchondritic S/Se consistent with its hydrothermal origin.

Apart from the chalcogens S, Se and Te, pyrite appears to be a minor contributor (<20%) of the whole-rock budget for both siderophile HSE (including Ni, Co and HSE) and chalcophile metals Ag, As, Au, Cu, Hg, Pb, Sb, Tl and Zn. The missing fraction of HSE occur as nanometer-sized particles (e.g. Ir-Os alloys), identified along with occasional detection of Mo and Re in half of the 52 analyzed crystals as well as outside pyrite, inside impact lithologies. These micronuggets are interpreted as variably altered remnants from repeated meteorite bombardment of the early martian crust. Nickel and cobalt are also impactor-derived, although now residing in solid solution in pyrite. Both elements, like chalcophile metals (e.g. As, Pb), are also present as trace elements dispersed in major minerals like pyroxene, Fe-Ti oxides or apatite (Humayun et al., 2013; Hewins et al., 2014c)

The chalcophile metal deficit can result from i) a high (>400°C) temperature crystallization for NWA 7533 pyrite, as deduced from its Se and Ni contents, ii) magmatic sulfide depletion of brecciated early martian crust, iii) precipitation from near neutral H_2S-HS-H_2O-rich hydrothermal fluids that did not provide halogen ligands for extensive transport of chalcophile-siderophile metals.

It is suggested that the 1.4 Ga lithification event that precipitated hydrothermal pyrite left the chalcophile-siderophile element budget of the early martian crust nearly unmodified, except for S, Se and Te.

Acknowledgments—We are indebted to L. Labenne for the sample. We are grateful for funding from CNES-INSU grant 2014-PNP (J.-P. L.). The LA-ICP-MS facility at the LPG Nantes was established by funds from the Region Pays de la Loire. Support by the NASA Solar System Workings program (NNX16AP98G) for research at FSU is acknowledged. The revised version was greatly improved thanks to comments from three reviewers and editorial suggestions of Rich Walker.

References

Abraitis P. K., Pattrick R. A. D., Vaughan D. J. (2004) Variations in the compositional, textural and electrical properties of natural pyrite: a review. *Intern. J. Miner. Process.* **74** 41– 59.

652 Agee C. B., Wilson N. V., McCubbin F. M., Ziegler K., Polyak V.J., Sharp Z. D., Asmerom Y.,
653 Nunn M. H., Shaheen R., Thiemens M. H., Steele A., Fogel M. L., Bowden R., Glamoclija
654 M., Zhang Z. and Elardo S. M. (2013) Unique meteorite from Early Amazonian Mars: water-
655 rich basaltic breccia Northwest Africa 7034. *Science* **339**, 780–785.
656
657 Arculus R. and Delano J. (1981) Siderophile element abundances in the upper mantle: evidence for
658 a sulfide signature and equilibrium with the core. *Geochim. Cosmochim. Acta* **45,**1331-1343.

659 Auclair G., Fouquet Y. and Bohn M. (1987) Distributions of selenium in high-temperature
660 hydrothermal sulfide deposits at 13° North, East Pacific Rise, *Can. Mineral.* **25**, 577-588.

661 Baumgartner R., Fiorentini M., Lorand J.-P., Baratoux D., Zaccarini F., Ferrière L., Prasek M. and
662 Sener K. 2017. The role of sulfides in the fractionation of highly siderophile and chalcophile
663 elements during the formation of martian shergottite meteorites. *Geochim. Cosmochim. Acta*
664 **210**, 1-24.

665 Barnes, H.L. (1979) Solubilities of ore minerals. In «Geochemistry of Hydrothermal Ore deposits»
666 (ed. H.L. Barnes), 404-460, John Wiley and Sons.

667 Barnes H. L. (2015) Hydrothermal processes. *Geochem. Persp.* **4**, pp. 1-93.

668 Barton P. B. (1970) Sulfide petrology. *Mineral. Soc. Amer. Special paper* **3**, 187-198.

669 Beck P., Pommerol, A., Remusat, L., Zanda, B., Lorand, J.-P., Göpel, C., Hewins, R., Pont, S.,
670 Lewin, E. , Quirico, E., Schmitt, B., Montes-Hernandez, G., Garenne, Bonal, L., Proux, O.,
671 Hazemann, J.L., Chevrier, V.C.F., 2015. Hydration of the dark meteorite and the red planet?
672 *Earth Planet. Sci. Lett* **427**, 104-111.

673 Bellucci J. J., Nemchin A. A., Whitehouse M. J., Humayun M., Hewins R. and Zanda B. (2015) Pb-
674 isotopic evidence for an early, enriched crust on Mars. *Earth Planet. Sci. Lett.* **410**, 34–41.

675 Bellucci J. J., Whitehouse M.J., John T., Nemchin A.A., Snape J.F., Bland P.A. and Benedix
676 G.K.(2017) Halogen and Cl isotopic systematics in Martian phosphates: Implications for the
677 Cl cycle and surface halogen reservoirs on Mars. *Earth Planet. Sci. Lett.* **458** 192–202 .
678
679 Brenan J. M., Cherniak D. J. and Rose L. A. (2000) Diffusion of osmium in pyrrhotite and pyrite:
680 implications forclosure of the Re-Os isotopic system. *Earth Planet. Sci. Lett.* **180**, 399-413.

681 Brenan J.M., Neil R. B. and Zajacz Z. (2016) Experimental Results on Fractionation of the Highly

682 Siderophile Elements (HSE) at Variable Pressures and Temperatures during Planetary and
683 Magmatic Differentiation. *Rev. Mineral. Geochem.* **81,** 1-87.
684
685 Cabri L. J. (1981) The platinum-group minerals. *In:* Platinum-Group Elements: Mineralogy,
686 Geology, Recovery. Cabri L. J. (ed). *Canad. Inst. Min. Metal.* **23**, p 84–150.
687
688 Cabri L. J., Harris D. C. and Weiser T.W. (1996) Mineralogy and distribution of the platinum-group
689 mineral (PGM) placer deposits of the world. *Explor. Min. Geol.* **5,** 73−167.
690
691 Campbell A. J., Simon S. B., Humayun M. and Grossman L. (2003) Chemical evolution of metal in
692 refractory inclusions in CV3 chondrites. *Geochim. Cosmochim. Acta* **67**, 3119–3134.
693
694 Capobianco C. J., Hervig R. L. and Drake M. J. (1994) Experiments on crystal/liquid partitioning of
695 Ru, Rh and Pd for magnetite hematite solid solutions crystallized from silicate melt. *Chem.*
696 *Geol.* **113,** 23–43.
697
698 Cassata W. S., Cohen B. E., Mark D. F., Trappitsch R., Crow C. A., Wimpenny J., Lee M. R. and
699 Smith C. L. (2018) Chronology of martian breccia NWA 7034 and the formation of the
700 martian crustal dichotomy. *Sci. Adv*. **4**, eaap8306, 11 pp.
701
702 Ciobanu C. L., Cook N. J. and Spry P. G. (2006) Preface – special issue: telluride and selenide
703 minerals in gold deposits – how and why? *Mineral. Petrol* **87**, 163–169.
704
705 Cook N.J., Ciobanu C.L., Wagner T. and Stanley C.J. (2007) Minerals of the system Bi-Te-Se-S
706 related to the tetradymite archetype: review of classification and compositional variation.
707 *Can. Mineral.* **45**, 665–708.
708
709 Dare SAS, Barnes S-J, Prichard HM and Fisher PC (2011) Chalcophile and platinum-group element
710 (PGE) concentrations in the sulfide minerals from the McCreedy East deposit, Sudbury,
711 Canada, and the origin of PGE in pyrite. *Mineral. Dep.* **46**, 381–407.
712
713 Day J. M. D., Brandon A. D. and Walker R. J. (2016) Highly siderophile elements in Earth, Mars,
714 the Moon, and asteroids. *Rev. Mineral. Geochem.* **81**, 161–238.

715 Deditius A.P., Reich M., Kesler S.E., Utsusomiya S., Chryssoulis S.L., Walshe J. and Ewing R.C.,
716 (2014) The coupled geochemistry of Au and As in pyrite from hydrothermal ore deposits.

717 *Geochim. Cosmochim. Acta* **140**, 644–670.

718 Dreibus G., Palme H., Spettel B., Zipfel J., Wänke H. (1995) Sulphur and selenium in chondritic
719 meteorites. *Meteoritics* **30**. 439−445.
720
721 Dressler B.O. and Reimold. W.U. (2001) Terrestrial impact melt rocks and glasses. *Earth-Science*
722 *Reviews* **56**, 205-284.

723
724 Duran C.J., Barnes S.-J. and Corkery J. T. (2015) Chalcophile and platinum-group element
725 distribution in pyrites from the sulfide-rich pods of the Lac des Iles Pd deposits, Western
726 Ontario, Canada: Implications for post-cumulus re-equilibration of the ore and the use of
727 pyrite compositions in exploration. *J. Geoch. Exp.* **158**, 223–242.
728
729 Einaudi M.T., Hedenquist J. W. and Esra Inan E. (2003) Sulfidation State of Fluids in Active and
730 Extinct Hydrothermal Systems: Transitions from Porphyry to Epithermal Environments
731 Giggenbach Volume, Society of Economic Geologists and Geochemical Society, Special
732 Publication 10 (S.F. Simmons, ed.).
733
734 Findlay A.J., Gartman A., Shaw T.J. and Luther G.W. III (2015) Trace metal concentration and
735 partitioning in the first 1.5 m of hydrothermal vent plumes along the Mid-Atlantic Ridge:
736 TAG, Snakepit, and Rainbow. *Chem. Geol.* **412**, 117–131.
737
738 Fischer-Gödde M., Becker H. and Wombacher F. (2010) Rhodium gold and other highly siderophile
739 element abundances in chondritic meteorites. *Geochim. Cosmochim. Acta* **74**, 356–379.
740 Funk C., Wormbacher F., Becker H., Bischoff D. , Günther D. and Mûnker C. (2015) Sulfur, Se
741 and Te abundances in chondrites and their components. Goldschmidt 2015 (abstract)

742 Genna D. and Gaboury D. (2015) Deciphering the hydrothermal evolution of a VMS system by
743 LA-ICP-MS using trace elements in pyrite: an example from the Bracemac-McLeod Deposits,
744 Abitibi, Canada, and implications for exploration. *Econ. Geol.* **110**, 2087–2108.

745 Gibert F., Pascal M. L. and Pichavant M. (1998) Gold solubility and speciation in hydrothermal
746 solutions; experimental study of the stability of hydrosulphide complex of gold (AuHS)° at
747 350 to 450° and 500 bars. *Geochim. Cosmochim. Acta* **62**, 2931-2947.

748 Goderis S., Paquay F. and Claeys Ph. (2012) Projectile identification in terrestrial impact structures

749 and ejecta material. In Impact cratering: processes and products (eds. G. R. Osinski and E.
750 Pierazzo), John Wiley & Sons Ltd, Chichester, UK. pp. 223–239. doi:
751 10.1002/9781118447307.ch15.

752 Goderis S., Brandon A. D., Mayer B. and Humayun M. (2016) Ancient impactor components
753 preserved and reworked in martian regolith breccia Northwest Africa 7034. *Geochim.*
754 *Cosmochim. Acta* **191**, 203–215.

755 Griffin W.L., Powell W.J., Pearson N.J. and O'Reilly S.Y. (2008) GLITTER: Data reduction
756 software for laser ablation ICP-MS: *Mineral Ass Can Short Course Series* 40, p. 308–311.
757

758 Grundler P. V., Brugger J., Etschmann B. E., Helm L., Liu W., Spry P. G., Tian Y., Testemale D. and
759 Pring A. (2013) Speciation of aqueous tellurium(IV) in hydrothermal solutions and vapors,
760 and the role of oxidized tellurium species in Te transport and gold deposition. *Geochim.*
761 *Cosmochim. Acta* **120**, 298–325.
762

763 Hannington M.D., Herzig P.M., Scott S., Thompson G. and Rona P. (1991) Comparative mineralogy
764 and geochemistry of gold-bearing sulfide deposits on the mid ocean ridges. *Marine Geology*
765 101, 217-248.

766 Hannington M. D., Herzig P. M. and Alt J. C. (1990) The distribution of gold in sub-seafloor
767 stockwork mineralization from DSDP hole 504B and the Agrokipia B deposit, Cyprus. *Can.*
768 *J. Earth Sci.* **27**, 1409-1417.

769 Harries D., Berg T., Langenhorst F. and Palme H. (2012) Structural clues to the origin of refractory
770 metal alloys as condensates of the solar nebula. *Met. Planet. Sci.* 47, 2148– 2159.

771 Helgeson H. (1970) A chemical and thermodynamic model of ore deposition in hydrothermal
772 systems. *Mineral. Soc. Amer. Special paper* **3**, 155-186.

773 Hewins R. H., Zanda B., Humayun M., Lorand J.-P., Deldicque D., Pont S., Fieni C., Nemchin A.,
774 Grange M., Kennedy A., Göpel C. and Lewin E. (2013) Petrology of NWA 7533: formation
775 by impacts on ancient martian crust. 76th Ann. Meet. Meteorit. Soc. Edmonton, Canada. *Met.*
776 *Planet. Sci.* #5252 (abstr.).

777 Hewins R. H., Zanda B., Humayun M., Nemchin A., Lorand J.-P., Pont S., Grange M., Kennedy A.,
778 Bellucci J. J., Whitehouse M., Beck P., Deldicque D., Göpel C., Remusat L., Lewin E. and
779 Pommerol A. (2014a) Ancient meteorite breccias from Mars. 77th Ann. Meet. Meteorit. Soc.

780 Casablanca, Morocco. *Met. Planet. Sci*. #5338 (abstr.).
781
782 Hewins R. H., Bourot-Denise M., Zanda B., Leroux H., Barrat J.-A., Humayun M., Göpel C.,
783 Greenwood R.C., Franchi I.A., Pont S., Lorand J.-P., Cournède C., Gattacceca J., Rochette P.,
784 Kugak M., Marrocchi Y., Marty B. (2014b) The Paris meteorite, the least altered CM
785 chondrite so far. *Geochim. Cosmochim. Acta* **124,** 190–222.

786 Hewins R. H., Zanda B., Humayun M., Lorand J.-P. and Pont S. (2014c) Impact melt rocks and
787 pristine clasts in Northwest Africa 7533. *Lunar Planet. Sci. Conf*. **45**, abstract #1416.

788 Hewins R. H., Zanda B., Humayun M., Nemchin A., Lorand J.-P., Pont S., Deldicque D., Bellucci
789 J. J., Beck P., Leroux H., Marinova M., Remusat L., Göpel C., Lewin E., Grange M., Kennedy
790 A.,Whitehouse M. (2017) Regolith breccia Northwest Africa 7533: Mineralogy and petrology
791 with implications for early Mars. *Met. Planet. Sci.* **52**, 89-124.

792 Humayun M., Nemchin A., Zanda B., Hewins R. H., Grange M., Kennedy A., Lorand J.-P., Göpel
793 C., Fieni C., Pont S., and Deldicque D. (2013) Origin and age of the earliest Martian crust
794 from meteorite NWA7533. *Nature* **503,** 513– 517.

795 Humayun M., Hewins R.H., Lorand J.-P. and Zanda, B. (2014). Weathering and impact melting
796 determined the mineralogy of the early Martian crust preserved in Northwest Africa 7533.
797 Lunar Planetary Institute, Houston. *XLV* #1880 (abstr.).
798
799 Huston D. L., Sie S. H., Suter G. F., Cooke D. R. and Both R. A. (1995) Trace elements in sulfide
800 minerals from eastern Australian volcanic-hosted massive sulfide deposits; Part I, Proton-
801 microprobe analyses of pyrite, chalcopyrite, and sphalerite, and Part II, selenium levels in
802 pyrite; comparison with $\delta^{34}S$ values and implications for the source of sulfur in
803 volcanogenic hydrothermal systems. *Econ. Geol*. **90**, 1167–1196.
804
805 Kaasalainen A., Stefánsson A., Giroud N. and Arnórsson S. (2015) The geochemistry of trace
806 elements in geothermal fluids, Iceland. *Appl. Geochem.* **62,** 207–223.
807
808 Keith M., Haase K. M., Klem R., Krumm S. and Strauss H. (2016) Systematic variations of trace
809 element and sulfur isotope compositions in pyrite with stratigraphic depth in the Skouriotissa
810 volcanic-hosted massive sulfide deposit, Troodos ophiolite, Cyprus. *Chem. Geol.* **423**, 7–18.
811
812 Koeberl, C., Claeys P., Hecht L. and McDonald I. (2012) Geochemistry of Impactites *Elements* **8**,

813 37–42

814 Large R.R., Maslenikov V.V., Robert F., Danyushevsky L.V. and Change, Z. (2007) Multistage
815 Sedimentary and Metamorphic Origin of Pyrite and Gold in the Giant Sukhoi Log Deposit,
816 Lena Gold Province, Russia. *Econ. Geol.* **102**, 1233–1267.
817
818 Leroux H., Jacob D., Marinova M., Hewins R. H., Zanda B., Pont S., Lorand J.-P., and Humayun
819 M. (2016) Exsolution and shock microstructures of igneous pyroxene clasts in the NWA
820 7533 Martian meteorite. *Met. Planet. Sci.* **51,** 932–945.

821 Lindsay, F. N., Turrin, B. D., Göpel, C., Herzog, G. F., Zanda, B., Hewins, R., Park, J., Delaney, J.
822 S. ans Swisher, C. C. (2014) $^{40}Ar/^{39}Ar$ Ages of Martian Meteorite NWA 7533. *Met. Planet.*
823 *Sci.*47, Abstract #5383.
824
825 Longerich H. P., Jackson S. E. and Günther D. (1996) Laser ablation inductively coupled plasma
826 mass spectrometric transient signal data acquisition and analyte concentration calculation.
827 *J. Anal. Atom. Spect.* **11**, 899–904.

828 Lorand J.-P. and Alard O. (2011) Pyrite tracks assimilation of crustal sulfur in some Pyrenean
829 lherzolites. *Mineral. Petrol.* **101**, 115-128.

830 Lorand J.-P., Alard O., Luguet A. and Keays R. R. (2003) S/Se systematics of the subcontinental
831 lithospheric mantle beneath the Massif Central. *Geochim. Cosmochim. Acta* **67**, 4137–4153.

832 Lorand J.-P., Alard O. and Luguet A. (2010) Platinum-group element micronuggets and
833 refertilization process in the Lherz peridotite. *Earth Planet. Sci. Lett.* **289**, 298-310.
834
835 Lorand J.-P., Hewins R. H., Remusat L., Zanda B., Pont S., Leroux H., Damien J., Humayun M.,
836 Nemchin A., Grange M., Kennedy A. and Göpel C. (2015) Nickeliferous pyrite tracks
837 pervasive hydrothermal alteration in Martian regolith breccias: a study in NWA 7533. *Met.*
838 *Planet. Sci.* **50**, 2099–2120.
839
840 Lorand J.-P., Luguet A., Alard O., Bézos A. and Meisel T. (2008) Abundance and distribution of
841 platinum-group elements in orogenic lherzolites; a case study in a Fontête Rouge lherzolite
842 (French Pyrenees). *Chem. Geol.* **248**, 174–194.
843
844 Lorand J.-P. and Luguet A., 2016. Chalcophile/siderophile elements in mantle rocks: trace elements
845 in trace minerals. *Rev. Mineral. Geochem.* **81**, 441-488.

Lorand J.-P., Pont S., Chevrier V., Luguet A., Zanda B. and Hewins, R. H., 2018. Petrogenesis of martian sulfides in the Chassigny meteorite. *Amer. Mineral.* **103**, 872-885.

Maslennikov V. V., Maslennikova S. P., Large R. R. and Danyushevsky L. V. (2009) Study of trace element zonation in vent chimneys from the Silurian Yaman-Kasy volcanic hosted massive sulfide deposit (Southern Urals, Russia) using laser ablation-inductively coupled plasma mass spectrometry (LA-ICPMS). *Econ. Geol.* **104**, 1111–1141.

McCubbin F. M., Boyce J. W., Novák-Szabó T., Santos A. R., Tartese R., Muttik N., Domokos G., Vazquez J., Keller L. P., Moser D. E., Jerolmack D. J., Shearer C. K., Steele A., Elardo S. M., Rahman Z., Anand M., Delhaye T. and Agee C. B. (2016) Geologic history of Martian regolith breccia Northwest Africa 7034: Evidence for hydrothermal activity and lithologic diversity in the Martian crust. *J. Geophys. Res. Planets* **121**, doi:10.1002/2016JE005143.

Murowchick J. B. and Barnes H. L. (1986) Marcasite precipitation from hydrothermal solutions. *Geochim. Cosmochim. Acta* **50**, 2615-2629.

Murowchick J. B. and Barnes H. L. (1987) Effect of temperature and degree of supersaturation on pyrite morphology. *Amer. Mineral.* **72**, 1241-1250.

Muttik N., McCubbin F.M., Keller L.P., Santos A.S., McCutcheon, M.C., Provencio P.P., Rahman Z., Shearer C.K., Boyce J.W. and Agee C.B. (2014). Inventory of H_2O in the ancient Martian regolith from Northwest Africa 7034: The important rôle of Fe oxides. *Geoph. Res. Lett.* **41**, 8235–8244.

Nan Li N., Deng J., Yang L.Q., Goldfarb R.J., Zhang C., Marsh E., Lei S.B., Koenig A. and Lowers H. (2014) Paragenesis and geochemistry of ore minerals in the epizonal gold deposits of the Yangshan gold belt, West Qinling, China. *Mineral. Dep.* **49**, 27–449

Nemchin A., Humayun M., Whitehouse M. J., Hewins R. H., Lorand J.-P., Kennedy A., Grange M., Zanda B., Fieni C. and Deldicque D. (2014) Record of the ancient martian hydrosphere and atmosphere preserved in zircon from a martian meteorite. *Nature Geoscience* **7**, 638–642.

O'Driscoll B. and González-Jiménez J.M. (2016) Petrogenesis of the Platinum-Group Minerals *Rev. Mineral. Geochem.* **81,** 489-578.

Pagé P., Barnes S.-J., Bedard J.H. and Zientek M.L. (2012) In-situ determination of Os, Ir, and Ru

in chromites formed from komatiite, tholeiite and boninite magmas: Implications for chromite control of Os, Ir and Ru during partial melting and crystal fractionation. *Chem. Geol.* **302**, 3–15.

Palme H. and Wlotzka F. (1976) A metal particle from a Ca–Al-rich inclusion for the meteorite Allende, and condensation of refractorysiderophile elements. *Earth Planet. Sci. Lett.* **33**, 45–60.

Palme H. and O'Neill H. S. C. (2014) Cosmochemical estimates of mantle composition. Holland HD and Turekian KK (eds.) *Treatise of Geochemistry*. 2nd edition. In: Carlson RW (ed.) The Mantle and Core, vol. 2, pp. 1–38. Oxford: Elsevier-Pergamon.

Patten C.G.C., Pitcairn I. K., Teagle D. A. H. and Harris M. (2016) Sulphide mineral evolution and metal mobility during alteration of the oceanic crust: Insights from ODP Hole 1256D. *Geochim. Cosmochim. Acta* **193,** 132–159.

Piña R., Gervilla F., Barnes S.-J., Ortega, L. and Lunar R. (2013) Platinum-group elements-bearing pyrite from the Aguablanca Ni-Cu sulphide deposit (SW Spain): a LA-ICP-MS study. *European Journal of Mineralogy* 25, 241-252.

Reich M., Kesler S.E., Utsunomiya S., Palenik C.S., Chryssoulis S.L., Ewin, R.C. (2005) Solubility of gold in arsenian pyrite. *Geochim. Cosmochim. Acta* **69**, 2781–2796.

Scher S., Williams Jones S.A. and Williams-Jones G. (2013) Fumarolic activity, acid-sulfate alteration, and high sulfidation epithermal precious metal mineralization in the crater of Kawah Ijen Volcano, Java, Indonesia. *Econ. Geol.* **108**, 1099–1118.

Seward T.M., Williams-Jones A.E. and Migdisov, A.A. (2014) The chemistry of metal transport and deposition by ore-forming hydrothermal fluids. *Treatise of Geochemistry*. Second Ed. 13, 29–57.

Seyfried W.E. and Ding K. (1995) Phase equilibria in subseafloor hydrothermal systems: a review of the role of redox, temperature, pH, and dissolved Cl on the chemistry of hot spring fluids and Mid-Ocean Ridges. In: Humphris, S.E., Zierenber, R.A., Mullineaux, L.S., Thomson, R.E. (Eds.), Seafloor Hydrothermal Systems: Physical, Chemical, Biological, and Geological Interactions. *American Geophysical Union*.

Shendberger D.M. and Barnes H.L. (1989) Solubility of gold in aqueous sulfide solutions from 150

913 to 350°C. *Geochim. Cosmochim. Acta* **53**, 269-278.
914
915 Sylvester P.J. (2008) Matrix effects in laser ablation-ICP-MS. *Mineral Ass Can Short Course Series*
916 40, Chapter 5 pp. 67-78.
917
918 Tagle and Berlin (2008). A database of chondrite analyses including platinum group elements, Ni
919 Co, Au, and Cr: Implications for the identification of chondritic projectiles. *Met. Planet. Sci.*
920 **43**, 541–559.
921
922 Schirmer T., Koschinsky A. and Bau M. (2014). The ratio of tellurium and selenium in geological
923 material as a possible paleo-redox proxy. *Geology* **376,** 44–51
924
925 Vaughan, D. and Craig, J.R. (1997) Sulfide ore mineral stabilities, morphologies and intergrowth
926 textures. In "Geochemistry of hydrothermal ore deposits, 3rd edn., edited by Barnes H.L..
927 New York: John Wiley and Sons, pp. 367-434.
928
929 Voudouris, P.C., Melfos V., Paul G. Spry, Moritz R., Papavassiliou C. and Falalakis G. (2011)
930 Mineralogy and geochemical environment of formation of the Perama Hill high-sulfidation
931 epithermal Au-Ag-Te-Se deposit, Petrota Graben, NE Greece. *Mineral. Petrol.* **103,** 79–100.
932
933 Wang Z. and Becker H. (2013) Ratios of S, Se and Te in the silicate Earth require a volatile-rich late
934 veneer. *Nature* **499**, 328–331.
935
936 Wasson J.T. and Kallemeyn G.W. (1988) Compositions of chondrites. *Philosophical Transaction*
937 *Royal Society of London* **A325**, 535-544.
938
939 Wilkin R. T. and Barnes H. L. (1997) Formation processes of framboidal pyrites. *Geochim.*
940 *Cosmochim. Acta* **61**, 323-339.
941
942 Wilson S.A., Ridley W.I. and Koenig, A.E. (2002) Development of sulfide calibration standards for
943 the laser ablation inductively-coupled plasma mass spectrometry technique. *J. Anal. At. Sp.*
944 **1**7, p. 406–409.
945
946 Wittmann A., Korotev R. L., Jolliff B. L., Irving A. J., Moser D., Barker I. and Rumble III, D.
947 (2015) Petrography and composition of Martian regolith breccia meteorite Northwest Africa
948 7475. *Met. Planet. Sci.* **50**, 326–352.

Wohlgemuth-Ueberwasser C., Viljoen F., Petersen S. and Vorster C. (2015) Distribution and solubility limits of trace elements in hydrothermal black smoker sulfides: An in-situ LA-ICP-MS study. *Geochim. Cosmochim. Acta* **159,** 16–41.

Wohlgemuth-Ueberwasser C. C., Ballhaus C., Berndt J., Stotter nee Paliulionyte V. and Meisel T. (2007) Synthesis of PGE sulfide standards for laser ablation inductively coupled plasma mass spectrometry (LA-ICP-MS). *Contrib. Mineral. Petrol.* **15**4, 607–617.

Yang S., Humayun M., Righter K., Jefferson G., Fields D. and Irving A. J. (2015) Siderophile and chalcophile element abundances in shergottites: implications for Martian core formation. *Met. Planet. Sci.***50**, 691–714.

Zhong R., Brugger J., Chen Y., Li W. (2015) Contrasting regimes of Cu, Zn and Pb transport in ore-forming hydrothermal fluids. *Chem. Geol.* **395**, 154–164

Figure captions:

Figure 1. Concentration profile of selected chalcophile-siderophile elements along the laser traverse through a lithic clast (Clast XIV). The HSE spikes are interpreted as submicrometer-sized nuggets that are evenly distributed in impact lithologies of NWA 7533. Some micronuggets are clearly offset from the concentrations peaks of S, Fe, Ni, Pb and Te corresponding to pyrite (Py).

Figure 2. Time-resolved LA-ICPMS spectra collected during four analyses of pyrites (count per second (cp/s) vs. time (s)). The spikes of PGE, Re and Mo concentrations are interpreted to be submicrometer-sized highly siderophile element (HSE)-rich nuggets intercepted by the laser beam. Log scale (left) for S; linear scale (right) for HSE micronuggets. Note that the four micronuggets show peak/background ratios > 30 (30 -1,000) that rule out any analytical artifact in their identification.

Figure 3. Ir vs. Pt and Pt vs. Mo diagrams for NWA 7533 pyrite. Insert: Ir and Pt-rich outliers. Note the broad positive correlation between Pt and Ir and the Mo enriched population in NWA 7533 pyrites. Carbonaceous chondrites (CI, CM, CK, CO); Ordinary chondrites (H); Enstatite chondrites (EH). Chondritic ratios after Wasson and Kallemeyn (1988); Tagle and Berlin (2008) and Palme and O'Neill (2014). Mix = pyrite +/- Fe oxyhydroxides. For error bars see Table S1.

Figure 4. Co vs. Ni diagram for NWA 7533 pyrite. EMPA: electron microprobe analyses. Other captions as in Fig. 3.

Figure 5. Se vs. Ni and Se vs. Te plots for NWA 7533 pyrite. CI-chondritic ratio after Wang and Becker (2013) and Palme and O'Neill (2014). Short dashed lines in Fig. 5B were arbitrarily drawn to delineate covariation trends between Se and Te. Note the overall Te enrichment with respect to chondritic Se/Te. CI chondrites after Wang and Becker (2013) and Palme and O'Neil (2014).

Figure 6. Plots of Pb and Bi vs. Te. Inserts: Pb-Bi-Te-rich outliers. Short dashed lines were arbitrarily drawn to delineate covariation trends between Pb and Te and Bi and Te. Note the Pb and Bi enrichements of mix analyses. Other captions as in Fig. 3.

Figure 7. Plots of Ga and Zn vs Sn. Note the positive correlation in Fig. 7A; the outliers in Fig. 7B correspond to mix analyses that incorporated significant amount of Fe-oxyhydroxides. Circle: Fe-(Ti) oxide. CI = CI-chondrites (Palme and O'Neill, 2004).

Figure 8. Concentration ranges of major and trace chalcophile-siderophile element concentrations in NWA 7533 pyrite (in bold) compared with terrestrial hydrothermal pyrite (thin grey lines). Terrestrial pyrite compositions after Abraitis et al. (2004), Large et al. (2007), Scher et al. (2013), Deditius et al. (2014), Li et al. (2014), Duran et al. (2015) and Patten et al. (2016). Note the logarithmic concentration scale.

Figure 9. Mass balance estimates of the contribution of pyrite to the whole-rock budget of NWA 7533 (whole-rock data after Humayun et al., 2013). Details of calculations in supplementary Table S5.

Figure 10: Log fO_2 vs. pH (A) and Log fO_2 vs. Log fS_2 (B) diagrams for the Fe-S-O system at T = 350°C displaying the concentrations of the different Au species dissolved in the putative hydrothermal fluids involved in the 1.4 Ga hydrothermal events (after Gibert et al., 1998). Black arrows delineate the range of redox conditions inferred for NWA 7533 (Lorand et al., 2015). Hm: hematite; Py: pyrite; Mt: magnetite; Po: pyrrhotite. The curves corresponding to kaolinite-illite (1) and K-feldspar (2) stability after Scher et al. (2013). Oxygen fugacity relative to the FMQ buffer after Lorand et al. (2015).

Figure

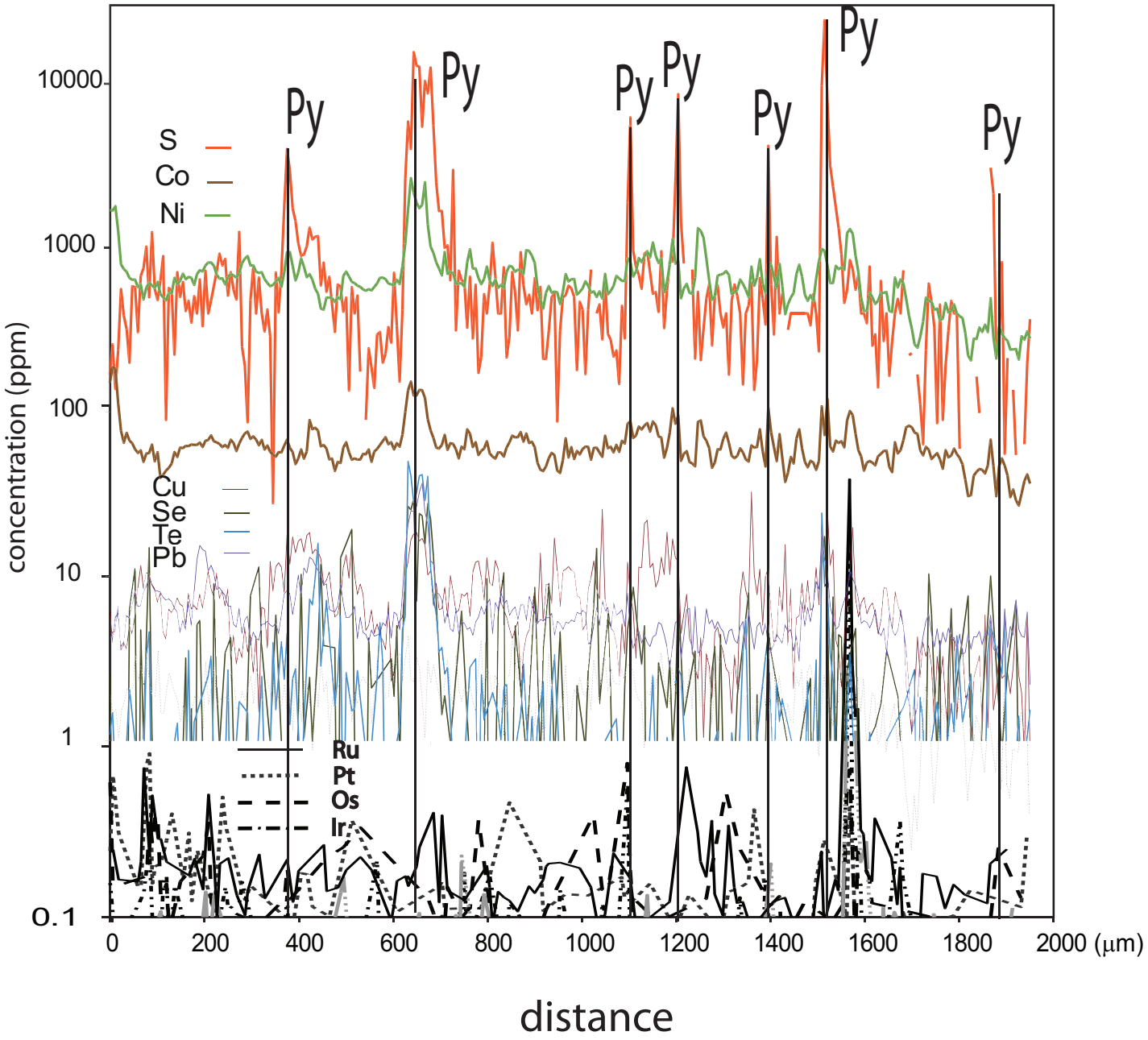
Py
Py
Py
Py
Py
Py
Py
S
Co
Ni
Cu
Se
Te
Pb
Ru
Pt
Os
Ir
10000
1000
100
10
1
0.1
concentration (ppm)
0
200
400
600
800
1000
1200
1400
1600
1800
2000 (μm)
distance

Fig. 1

Figure

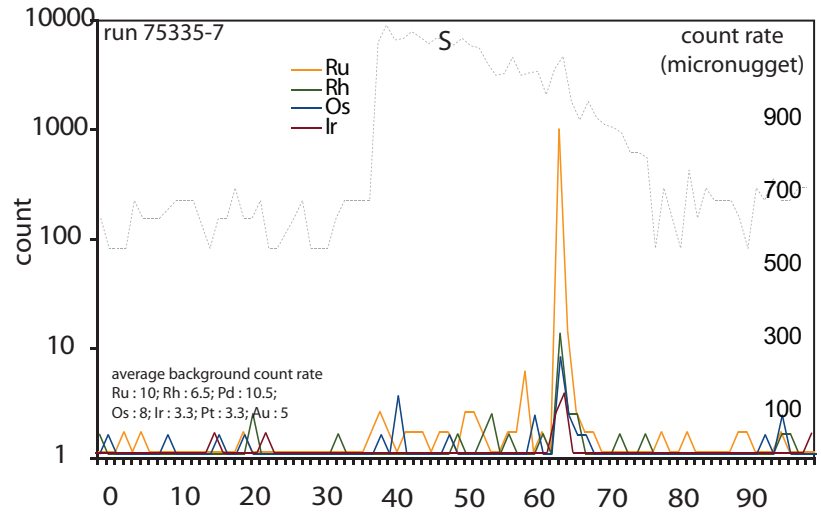
run 75335-7
S
count rate
(micronugget)
Ru
Rh
Os
Ir
count
average background count rate
Ru : 10; Rh : 6.5; Pd : 10.5;
Os : 8; Ir : 3.3; Pt : 3.3; Au : 5

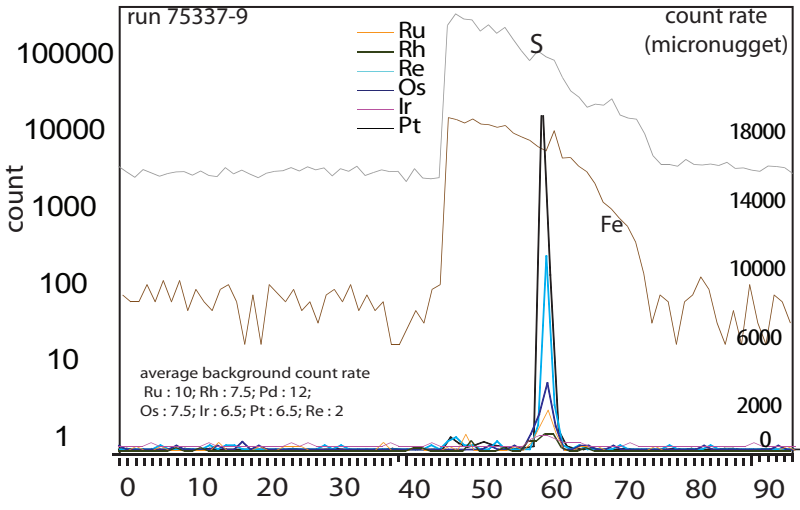
run 75337-9
S
Fe
count rate
(micronugget)
Ru
Rh
Re
Os
Ir
Pt
count
average background count rate
Ru : 10; Rh : 7.5; Pd : 12;
Os : 7.5; Ir : 6.5; Pt : 6.5; Re : 2

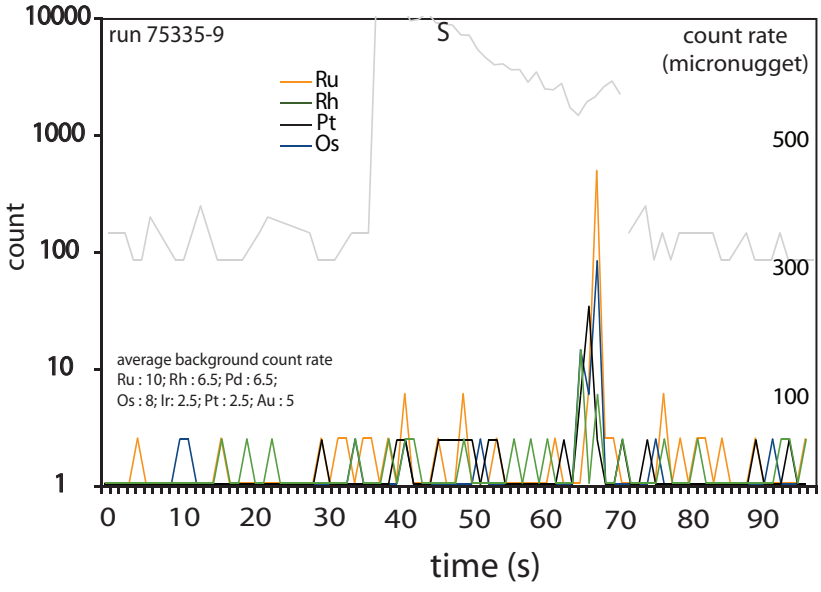
run 75335-9
S
count rate
(micronugget)
Ru
Rh
Pt
Os
count
average background count rate
Ru : 10; Rh : 6.5; Pd : 6.5;
Os : 8; Ir: 2.5; Pt : 2.5; Au : 5
time (s)

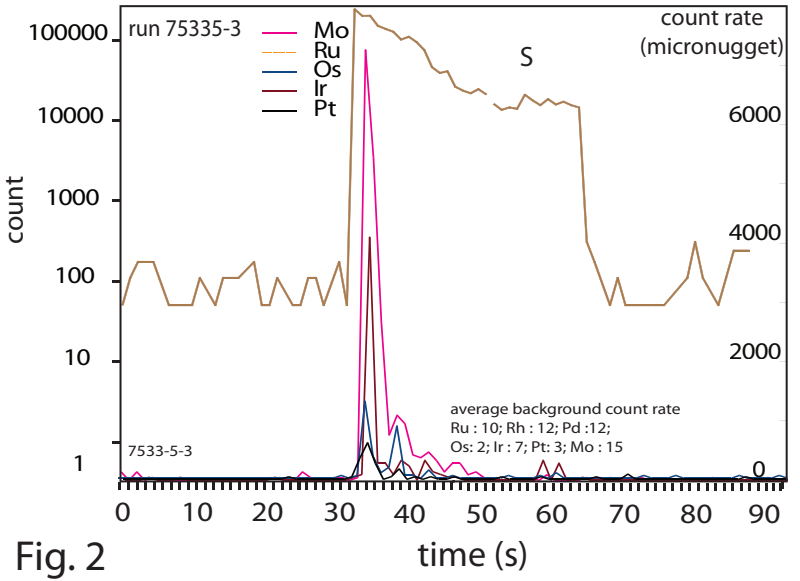
run 75335-3
Mo
Ru
Os
Ir
Pt
S
count rate
(micronugget)
count
7533-5-3
average background count rate
Ru : 10; Rh : 12; Pd :12;
Os: 2; Ir : 7; Pt: 3; Mo : 15
time (s)

Fig. 2

Figure

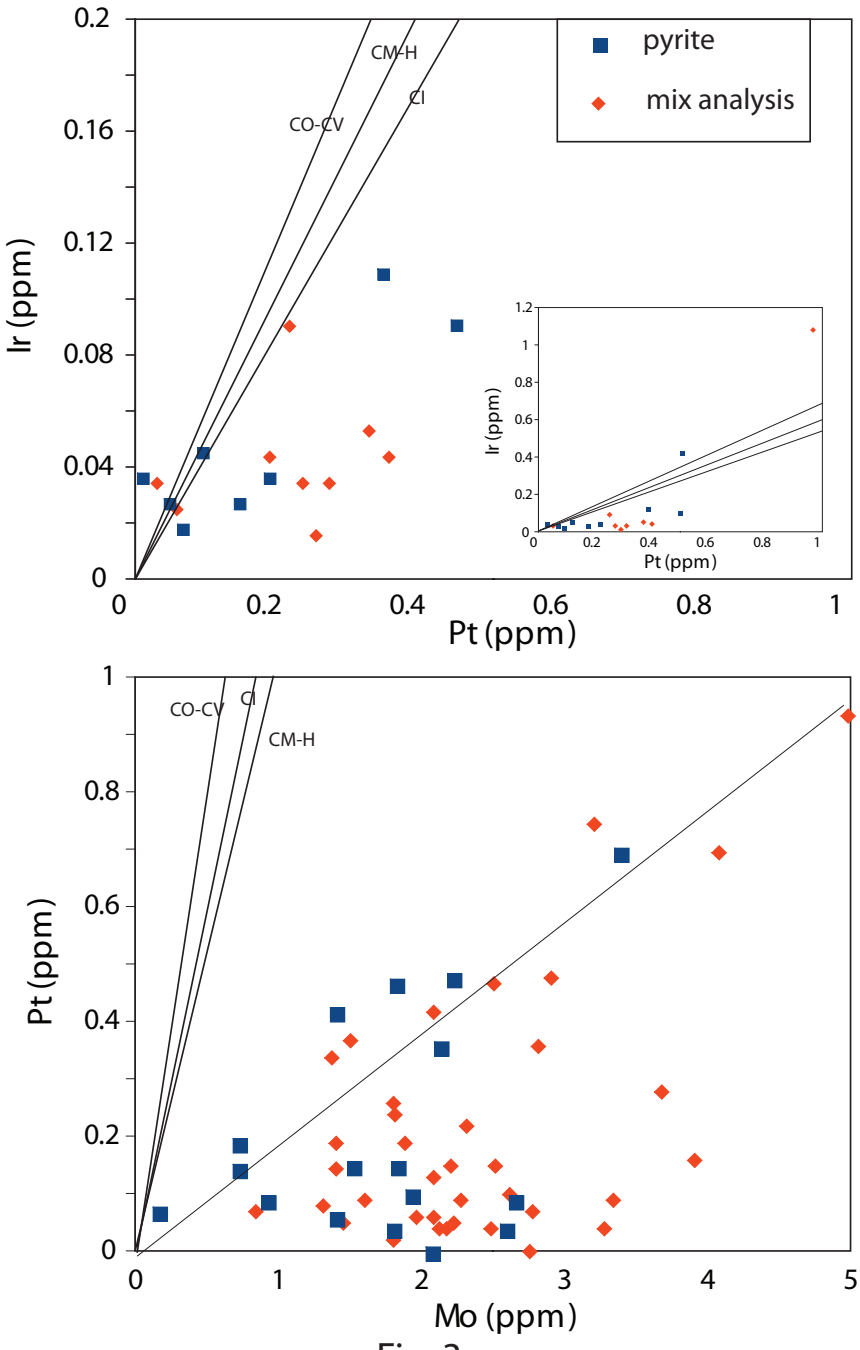
pyrite
mix analysis
CM-H
CI
CO-CV
Ir (ppm)
Pt (ppm)
0.2
0.16
0.12
0.08
0.04
0
0
0.2
0.4
0.6
0.8
1
1.2
CO-CV
CI
CM-H
Pt (ppm)
Mo (ppm)
0
1
2
3
4
5

Fig. 3

Figure

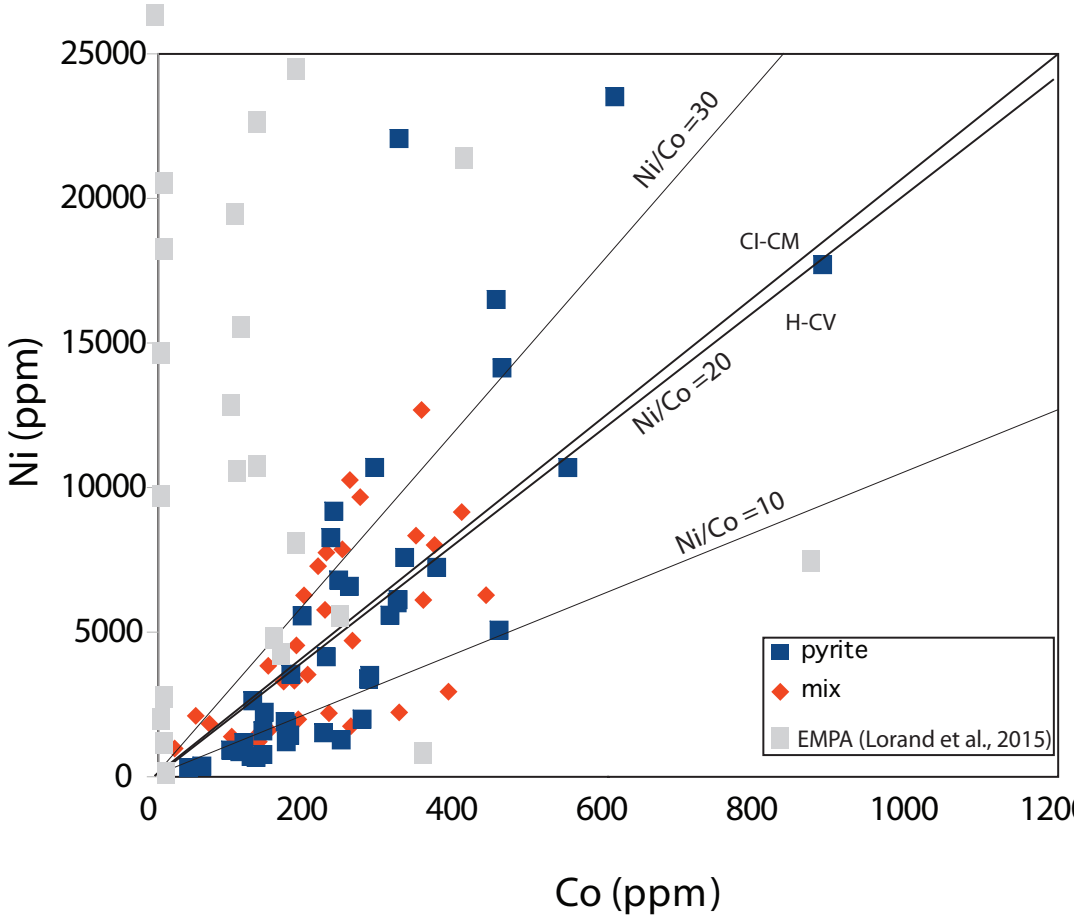
25000
20000
15000
10000
5000
0
Ni (ppm)
0
200
400
600
800
1000
1200
Co (ppm)
Ni/Co =30
CI-CM
H-CV
Ni/Co =20
Ni/Co =10
pyrite
mix
EMPA (Lorand et al., 2015)

Fig. 4

Figure

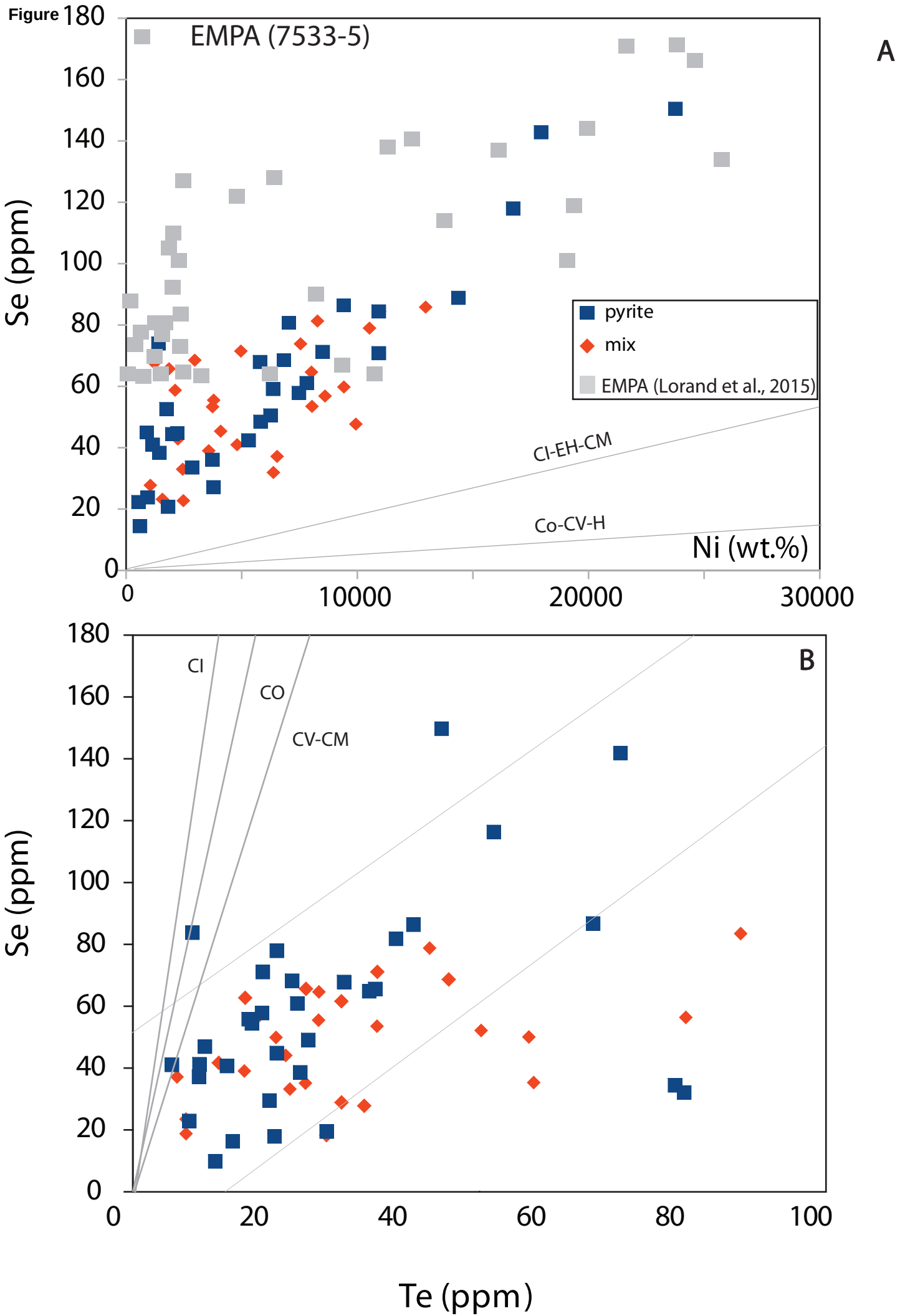
EMPA (7533-5)
A
Se (ppm)
180
160
140
120
100
80
60
40
20
0
pyrite
mix
EMPA (Lorand et al., 2015)
CI-EH-CM
Co-CV-H
Ni (wt.%)
0
10000
20000
30000
B
CI
CO
CV-CM
Se (ppm)
Te (ppm)
0
20
40
60
80
100

Figure

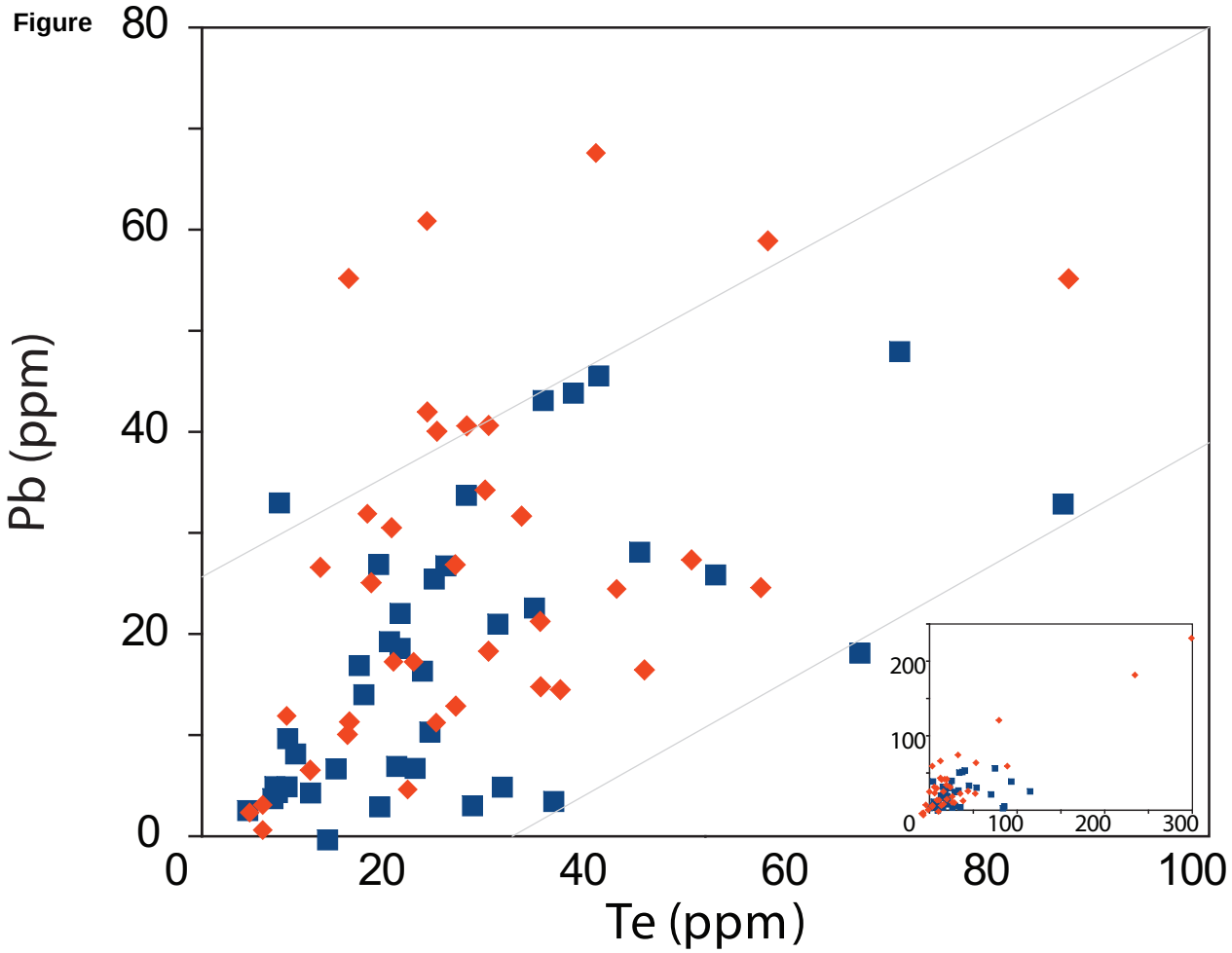
Pb (ppm)
Te (ppm)
0
20
40
60
80
100
200
300

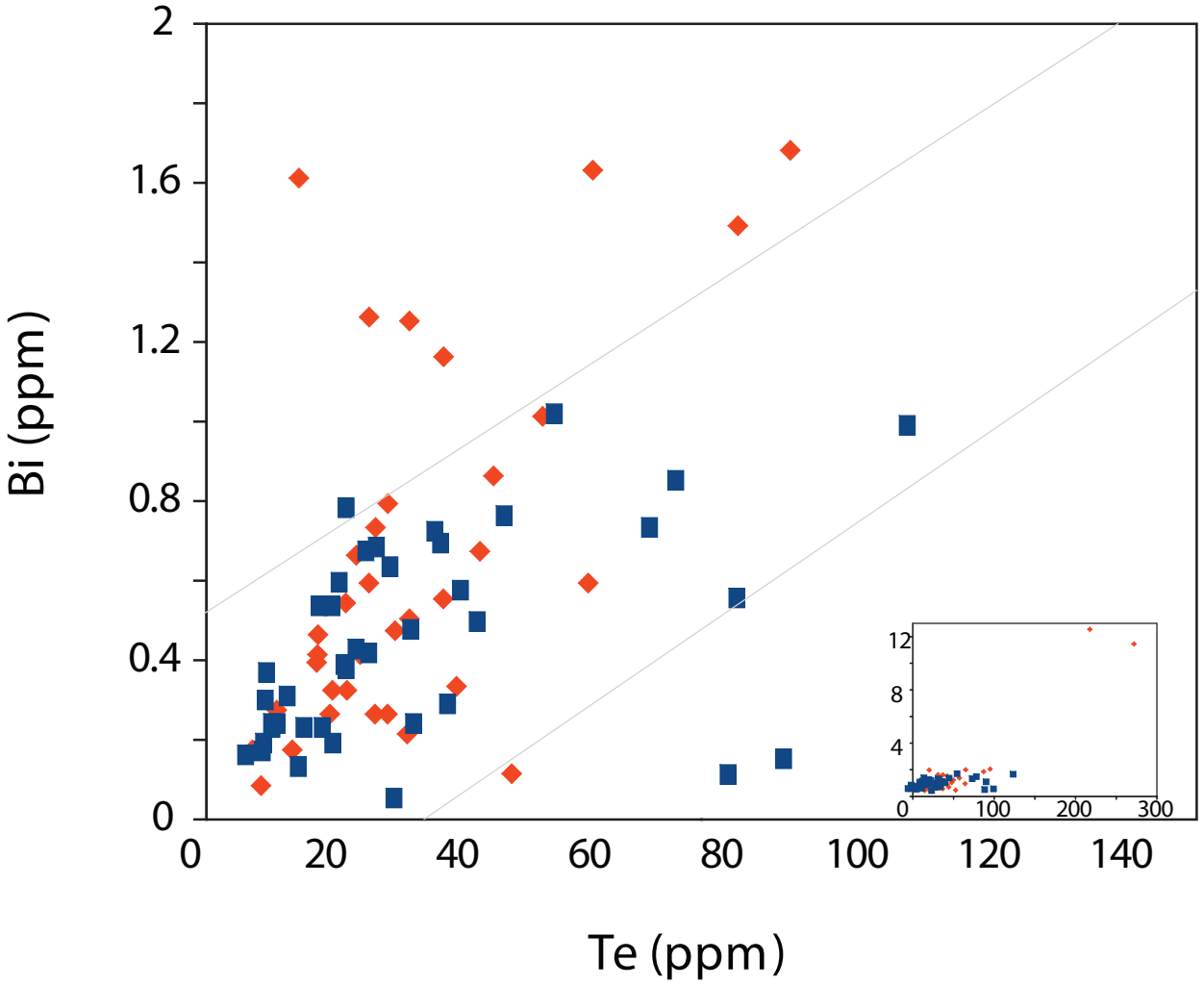
Bi (ppm)
Te (ppm)
0
0.4
0.8
1.2
1.6
2
20
40
60
80
100
120
140
4
8
12
200
300

Fig. 6

Figure

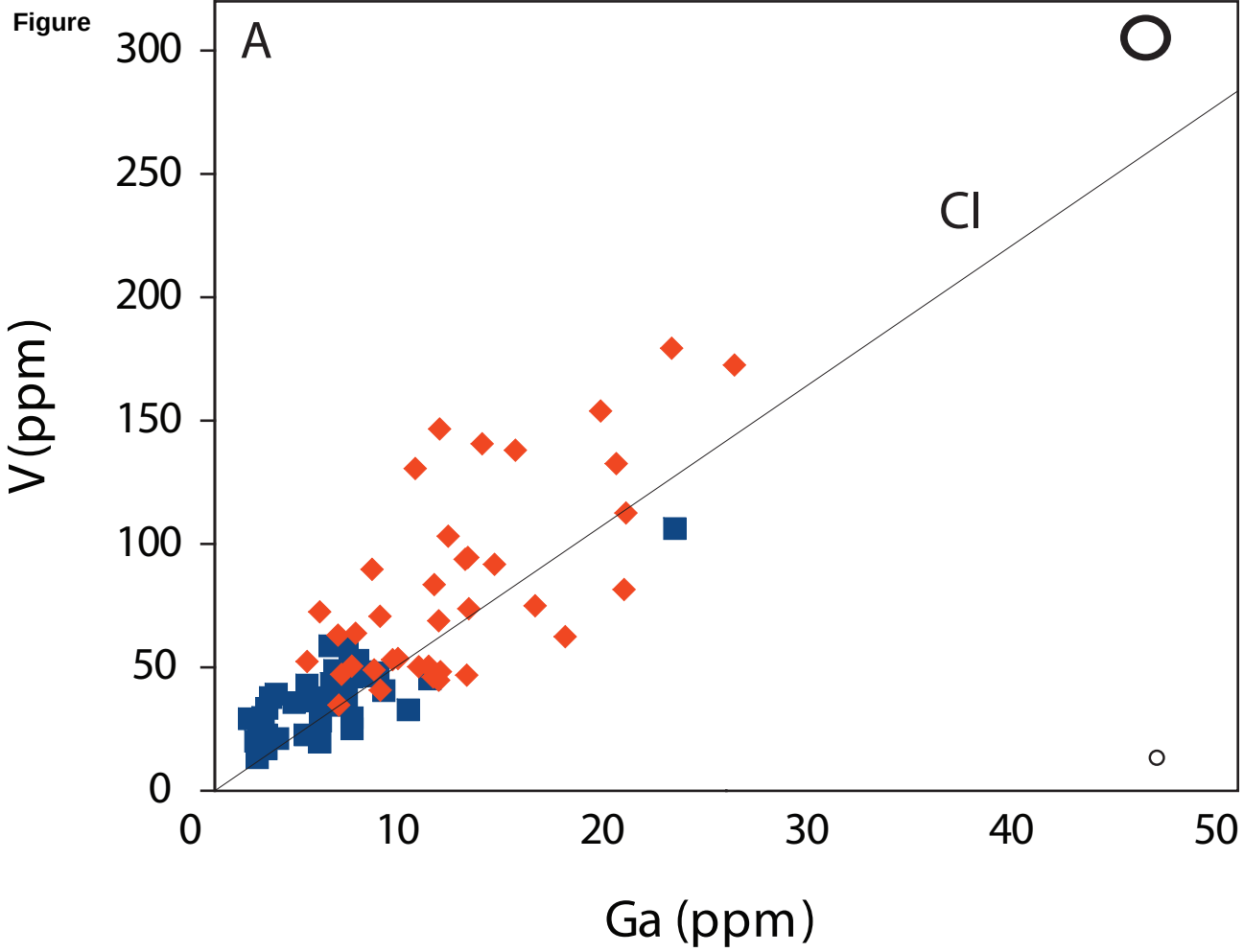
A
Cl
V(ppm)
Ga (ppm)
0
50
100
150
200
250
300
0
10
20
30
40
50

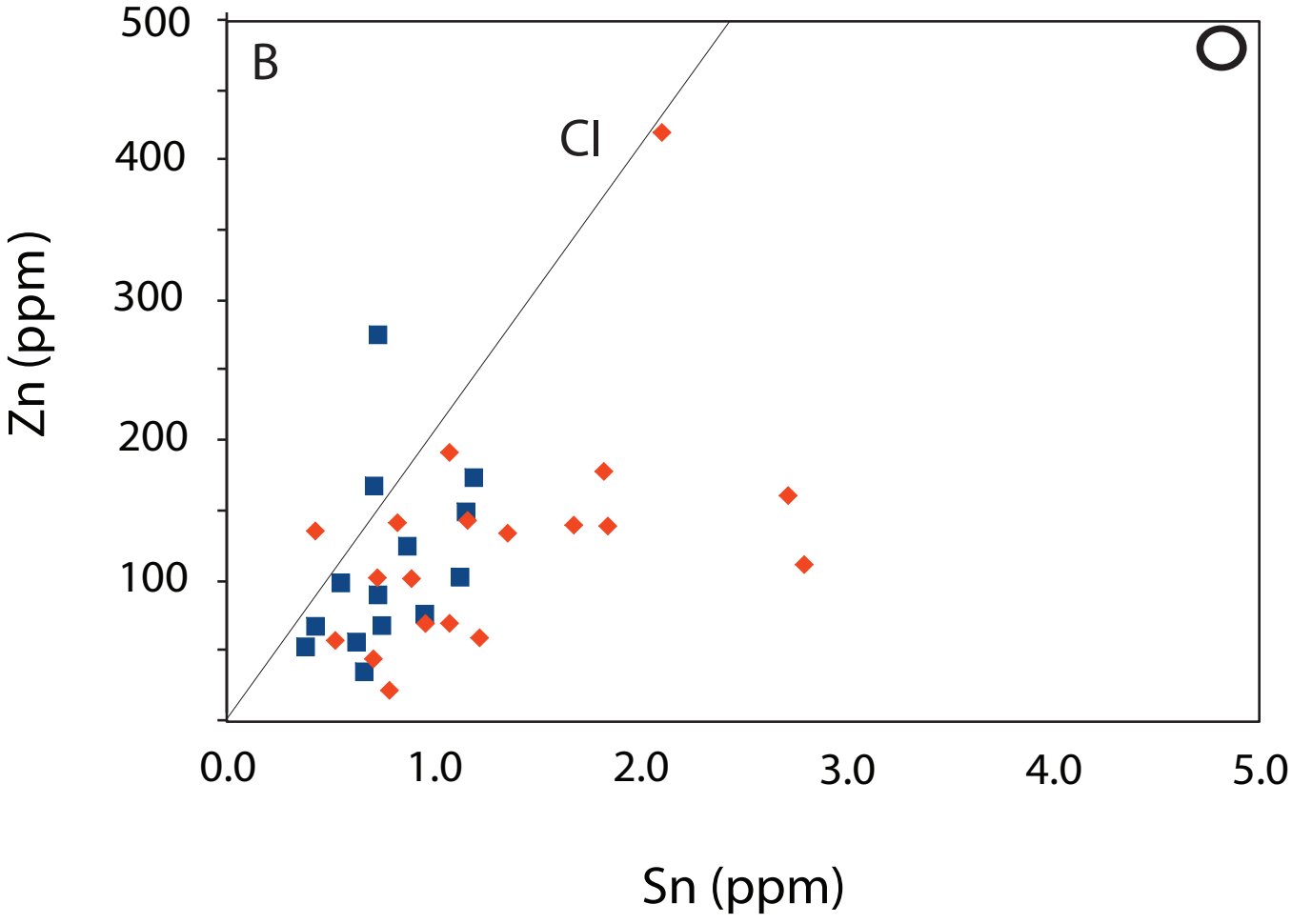
B
Cl
Zn (ppm)
Sn (ppm)
100
200
300
400
500
0.0
1.0
2.0
3.0
4.0
5.0

Fig. 7

Fig. 8

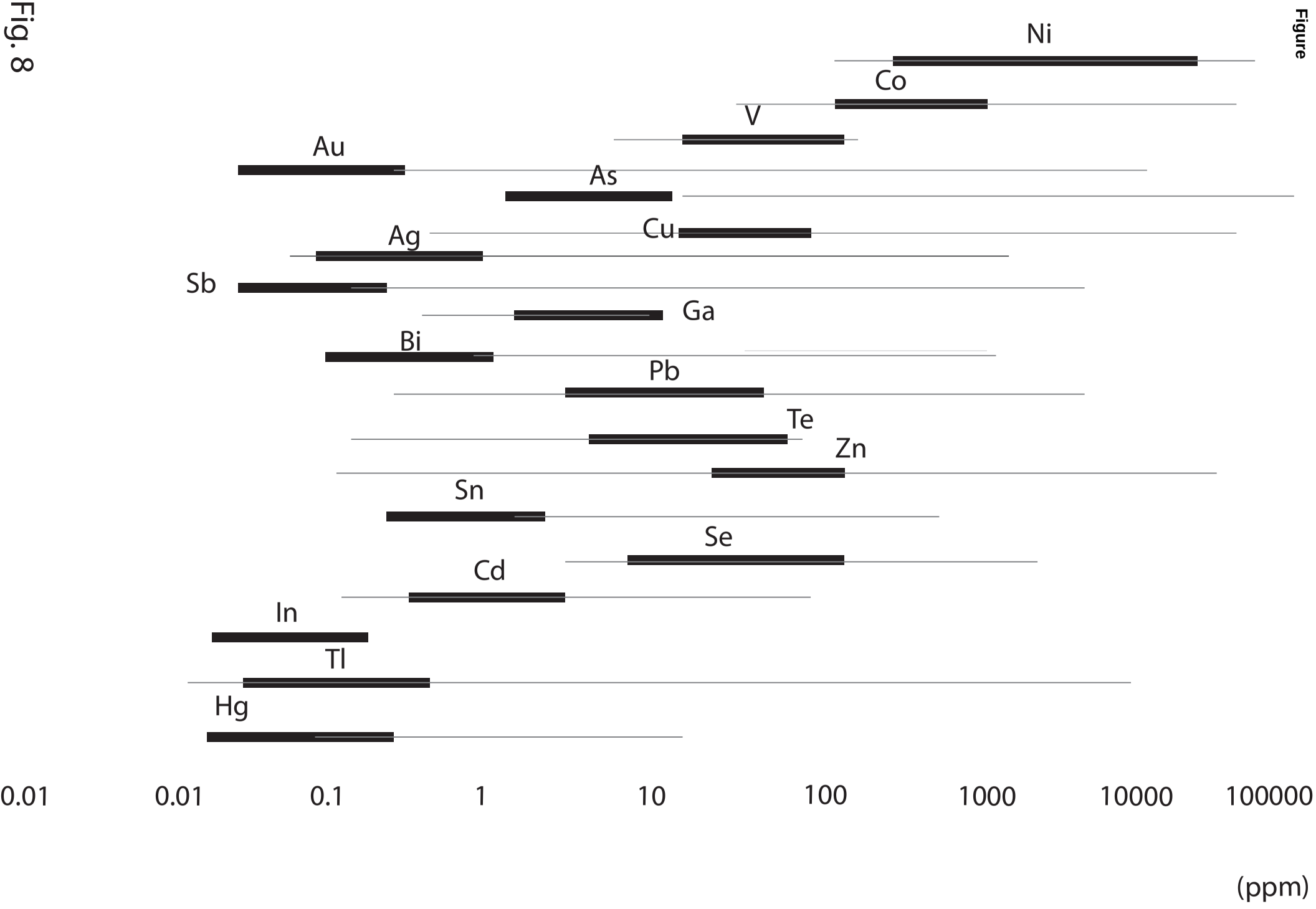
Ni
Co
V
Au
As
Ag
Cu
Sb
Ga
Bi
Pb
Te
Zn
Sn
Se
Cd
In
Tl
Hg
0.01
0.01
0.1
1
10
100
1000
10000
100000
(ppm)

Figure

Figure

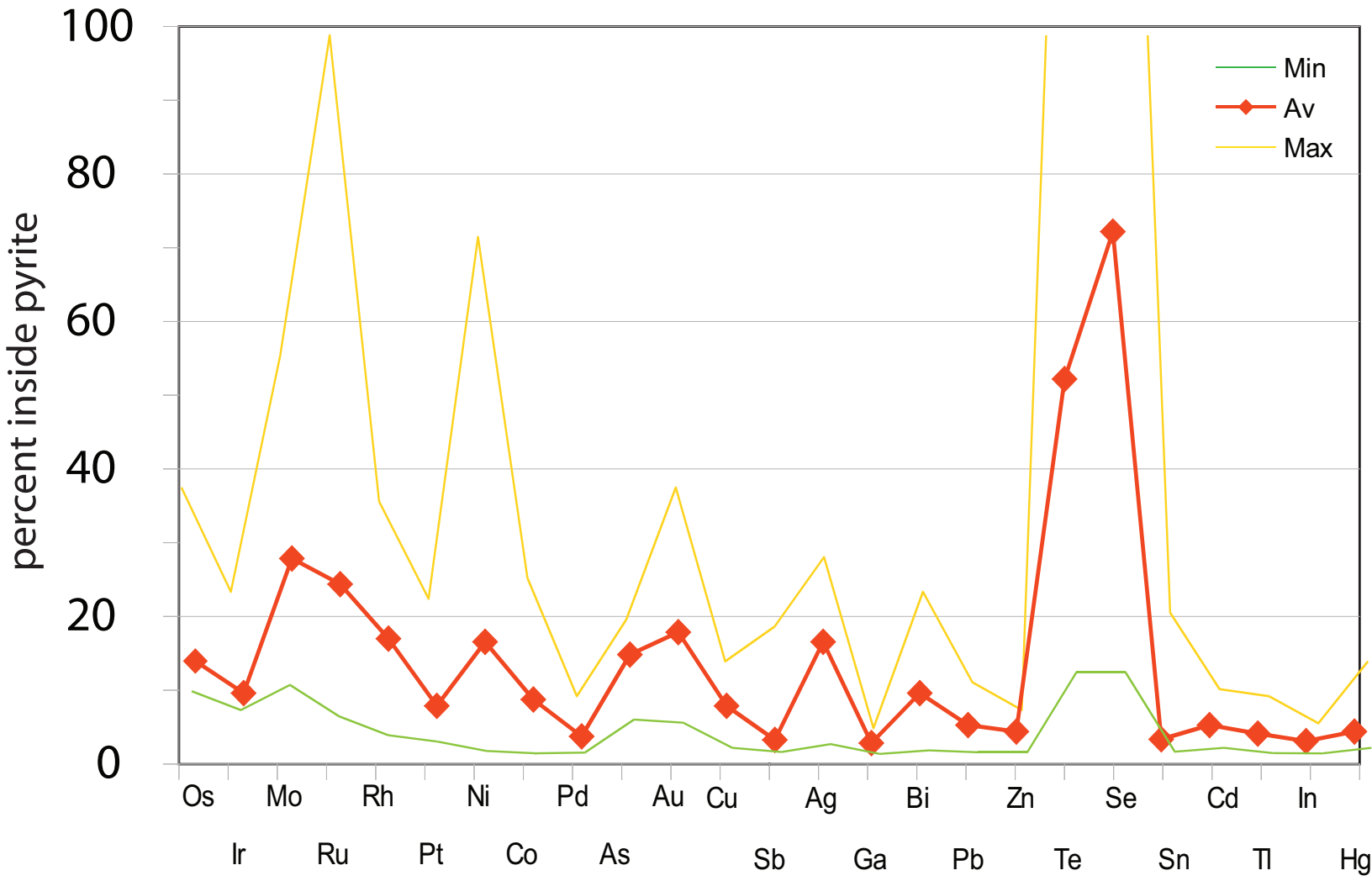
100
80
60
40
20
0
percent inside pyrite
Min
Av
Max
Os
Ir
Mo
Ru
Rh
Pt
Ni
Co
Pd
As
Au
Cu
Sb
Ag
Ga
Bi
Pb
Zn
Te
Se
Sn
Cd
Tl
In
Hg

Fig. 9

Figure

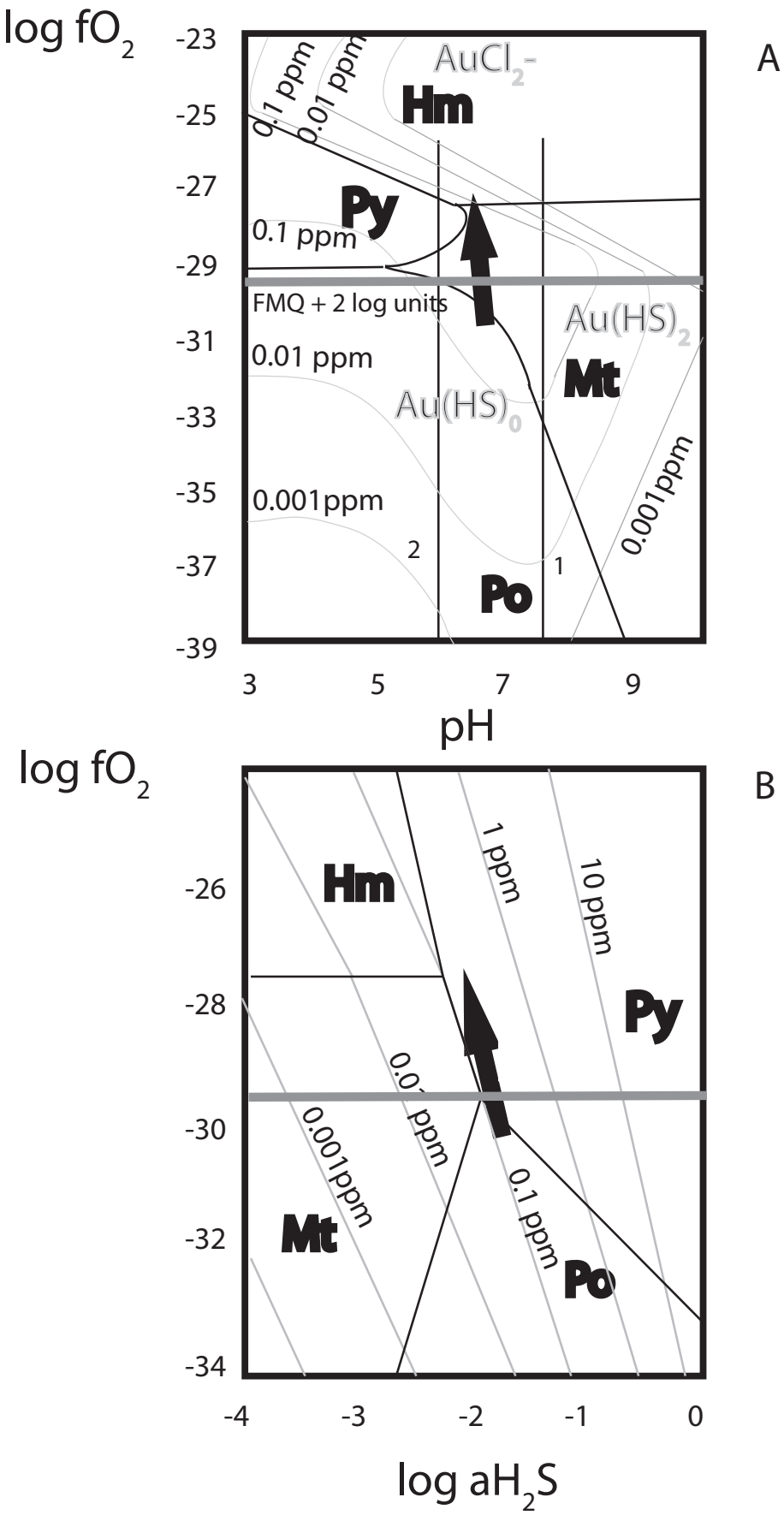

Fig. 10